Efficient simultaneous removal enrofloxacin and Cr(VI) via activation of peroxymonosulfate over defect-rich C-MoS$_2$-Fe

Jingyu Liu [a,b], Yongyou Hu [a,b,*], Xian Li [a,b,d], Chun Xiao [a,b], Bowen Yuan [a,b], Jianhua Cheng [a,b], Yuancai Chen [a,b], Xiaoqiang Zhu [b,c], Guobin Wang [c], Jieyun Xie [c]

[a] School of Environment and Energy, South China University of Technology, Guangzhou Higher Education Mega Centre, Guangzhou 510006, PR China
[b] The Key Lab of Pollution Control and Ecosystem Restoration in Industry Clusters, Ministry of Education, South China University of Technology, Guangzhou Higher Education Mega Centre, Guangzhou 510006, PR China
[c] Guangzhou Pengkai Environment Technology Co., Ltd, Guangzhou 511493, PR China
[d] School of Civil and Architecture Engineering, Nanchang Institute of Technology, Nanchang 330099, PR China

ARTICLE INFO

ABSTRACT

Carbon-doped MoS$_2$-Fe (C-MoS$_2$-Fe-x) was synthesized induced by the introduction of ethylene glycol using hydrothermal method. Benefitting from the synergistic effect of 1 T/2 H mixed phase and abundant defects, C-MoS$_2$-Fe-x had an excellent ability to simultaneous remove enrofloxacin (ENR) and Cr(VI) via peroxymonosulfate (PMS) activation (C-MoS$_2$-Fe-x/PMS). The most effective C-MoS$_2$-Fe-2/PMS showed a removal rate constant of 0.200 min^{-1} and 0.110 min^{-1} for ENR and Cr(VI), which were 15.4 and 8.5 times as high as those of the MoS$_2$-Fe/PMS, respectively. Combined with quenching experiments, electron paramagnetic resonance (EPR), and electrochemical experiments, singlet oxygen and electron-transfer can be illustrated for synergistic removal. C-MoS$_2$-Fe-2 exhibits high mineralization capacity and is structurally stable in use with minimal metal leaching. It is noteworthy that C-MoS$_2$-Fe-2/PMS displayed an outstanding purification effect on real pharmaceutical wastewater. This work provides new ideas for designing efficient and green non-homogeneous catalysts for Fenton-like systems to deal with composite pollution wastewater.

1. Introduction

In recent years, the environmental pollution resulting from organic compounds and toxic heavy metals in water has attracted more and more attention. Pharmaceutical wastewater is a serious water pollution, owing to its high toxicity, difficult degradation, and persistent [1,2]. Enrofloxacin (ENR) is a third-generation fluoroquinolone antibiotic with a good bactericidal effect, mainly used in healthcare, animal husbandry, and agriculture [3]. Moreover, Cr(VI) is regarded as a toxic heavy metal ion, exhibiting highly toxic and carcinogenic effects in humans and animals at very low concentrations [4]. The co-existence of Cr(VI) and antibiotics is a common phenomenon in pharmaceutical wastewater [5, 6]. Due to their different molecular structures and physicochemical properties, it is difficult to remove them simultaneously and effectively. Currently, techniques for removing Cr(VI) and antibiotics include adsorption, biodegradation, and chemical precipitation [7,8]. However, these techniques for removing complex pollutants have the disadvantage of being less efficient and prone to secondary contamination. Therefore, it is necessary to develop a green and efficient treatment technology to achieve simultaneous removal of ENR and Cr (VI) efficiently.

Persulfate-based Fenton-like reactions were regarded as an effective technology on simultaneous removal antibiotics and Cr(VI) [9–11]. The generated reactive oxygen species (ROSs), including sulfate (SO$_4^{\bullet-}$), hydroxyl (•OH), peroxide (•O$_2^-$) radicals, and singlet oxygen (^{1}O$_2$) are used for the degradation of organic pollutants [12,13]. While the abundance of electrons and Fe^{2+} promotes the reduction of Cr(VI) [14, 15]. Co-based catalysts are considered as the main activators for PMS activation. However, the leaching of highly toxic Co^{2+} is still unavoidable, which seriously influences its long-term practical applications [16, 17]. It is necessary to develop a catalyst with excellent performance and low toxicity.

MoS$_2$-Fe has received great attention due to its low toxicity as well as good robustness and durability to sustain PMS activation [18–21]. MoS$_2$

---

can promote the reduction of Fe^{3+} to Fe^{2+} through the oxidation of Mo^{4+} to Mo^{6+}. Dong et al. prepared MoS_2-Fe using a hydrothermal method for the removal of organic pollutants by activated PMS [22]. Despite showing good PMS activation ability, the reaction process required additional energy or the addition of a large amount of PMS. In addition, the performance of MoS_2-Fe activated PMS in the reduction of Cr(VI) is limited. This may be attributed to the poor electrical conductivity, low electron transport capacity, and limited active sites of MoS_2 [23].

It has been reported that defects were essential in modulating the catalytic property of metal sulfides [24,25]. Sulfur defects in MoS_2 not only increase the exposure of Mo active sites and facilitate the reduction of Fe^{3+} to Fe^{2+}, but also directly activate PMS to generate large amounts of $^1O_2$ [26]. It was shown that introducing carbon atoms into MoS_2 not only constructs abundant defects to increase the amount of active sites, but also induces the transfer of 2 H phase MoS_2 to 1 T phase, and the mixed-phase MoS_2 has a better electrical conductivity. Tian et al. prepared C-MoS_2 using a hydrothermal method, which demonstrated excellent hydrogen precipitation activity [27]. Therefore, carbon doping Fe-MoS_2 has great potential in activating PMS for simultaneous removal antibiotics and Cr(VI).

Herein, ethylene glycol-induced carbon-doped MoS_2-Fe (C-MoS_2-Fe-x) was ingeniously designed as catalysts to activate peroxymonosulfate (C-MoS_2-Fe-x/PMS) for simultaneous removal of ENR and Cr(VI). Ethylene glycol was used as both a carbon source and morphology modifier to control the catalyst formation. The performance of catalysts activated PMS for efficient decontamination was investigated using Density Functional Theory (DFT) calculations and experiments. The synergistic effects of 1 T/2 H mixed phase and abundant sulfur defects on improving the catalyst performance were systematically investigated by quenching experiments, EPR tests, and electrochemical experiments. The reusability and stability of the catalysts were evaluated. In addition, the effectiveness of the system on actual pharmaceutical wastewater was assessed. This study gives new ideas for the development of efficient non-homogeneous catalysts and new strategies for their use in Fenton-like technologies to improve the efficacy of the treatment of composite polluted wastewater.

2. Materials and methods

The information of materials and water samples involved in the experiment, catalyst characterization, measurement of ENR concentration and its intermediates, measurement of Cr(VI) concentration, measurement of PMS concentration, radical species measurement, toxicity tests, and analytic methods were listed in Text S1 and Text S3–8 (details in the Supplementary Material).

2.1. Synthesis of C-MoS₂-Fe-x

Typically, 0.5 mmol $(NH_4)_6Mo_7O_{24}\cdot4H_2O$, 20 mmol $CS(NH_2)_2$, and 0.1 mmol $FeSO_4\cdot7H_2O$ were added in a 40 mL mixture solution of ethylene glycol and water. After stirring for 2 h, the homogeneous solution was transferred to an autoclave then heated to 210 °C for 24 h. After centrifugation, the obtained products were washed using distilled water and ethanol. The yielded sample was obtained after being vacuum-dried at 80 °C overnight, and it is denoted as C-MoS_2-Fe-x. Herein, x = 1, 2, and 3, respectively, corresponding to different ethylene glycol-to-water volume ratios (1:1, 2:1, and 3:1). Additionally, MoS_2, C-MoS_2-2, and MoS_2-Fe were synthesized using similar methods to C-MoS_2-Fe-x, more information was exhibited in Text S2.

2.2. Evaluation of catalytic activity

The removal of ENR and Cr(VI) was used to evaluate the catalytic activity of the samples. 20 mg of catalyst is added to a solution (100 mL) containing ENR (10 mg L^{-1}) and Cr(VI) (5 mg L^{-1}). The mixture was

stirred at room temperature for 30 min to reach adsorption equilibrium. Then PMS was added to start the reaction. 1 mL sample was collected at regular intervals while quencher of methanol (0.1 mL) was added, and then filtered. 1 M H_2SO_4 and NaOH were employed for the pH adjustment.

2.3. Theoretical calculations

DFT calculations are performed using first principles in the generalized gradient approximation (GGA) using the Perdew-Burke-Ernzerhof (PBE) [28] formulation. A projection-enhanced wave (PAW) [29,30] potential is used to describe the ionic core and valence electrons are taken into account using a plane-wave basis set with a kinetic energy cut-off of 520 eV. The GGA+*U* method was used for the calculations. The effective Hubbard U value for molybdenum was set to 4.814 eV, and the Gaussian smearing method was used to allow for partial occupancy of the Kohn-Sham orbitals with a width of 0.05 eV. The electron energies are considered to be self-consistent when the energy variation is less than 10^{-6} eV. The geometry optimization is considered to be convergent when the energy change is less than 0.05 eV Å^{-1}. The Brillouin zone integrals were sampled for one structure using the $2 \times 2 \times 1$ Monkhorst-Pack k-point sampling method. Finally, the energy of adsorption (Eads) was calculated as $E_{ads} = E_{ad/sub} - E_{ad} - E_{sub}$, where $E_{ad/sub}$, E_{ad}, and E_{sub} are the total energy of the optimized adsorbent/substrate system, the adsorbent in the structure, and the clean substrate, respectively.

Fukui function calculations were used to predict the vulnerable sites on ENR molecules, more information about specific calculation methods was found in Text S9.

3. Results and discussion

3.1. Characterizations of C-MoS₂-Fe-x

The preparation of C-MoS_2-Fe-x is carried out by a hydrothermal method via adjusting the volume ratio of ethylene glycol and water (Fig. 1a). In this process, ethylene glycol is involved in the reaction as a carbon source and reducing agent. The quantity of carbon in C-MoS_2-Fe-x was listed in Table S1, the carbon content increased as ethylene glycol dosage increased. In addition, ethylene glycol as a reducing agent can slow down the release of S, which is favorable to the formation of C-MoS_2-Fe-x morphology.

SEM and HRTEM were used to observe the morphologies and microstructures of the catalysts. C-MoS_2-Fe-x showed spherical-like nanostructures composed of nanosheets (Fig. 1b-c and Fig. S1). Moreover, as the $V_{\text{ethylene glycol}}$: V_{water} increases from 1:1, 2:1 to 3:1, the particle diameter of the resulting C-MoS_2-Fe-x increases from 430 (C-MoS_2-Fe-1), 500 (C-MoS_2-Fe-2) to 640 nm (C-MoS_2-Fe-3). This may be due to the addition of ethylene glycol, which alters the diffusive and reactive action of the reagents [31,32]. The TEM image (Fig. 1d, represented by C-MoS_2-Fe-2) also shows that the nanosphere is assembled from nanosheets. Moreover, the elemental mapping analyses reveal that Mo (Fig. 1d₁), S (Fig. 1d₂), C (Fig. 1d₃), and Fe (Fig. 1d₄) elements distribute homogeneously throughout the nanosphere. The HRTEM image in Fig. 1e revealed that the interlayer spacing was 0.94 nm and 0.62 nm for the 1 T phase (002) and 2 H phase (002), respectively [33,34]. Furthermore, the interruption of the crystal streaks suggested the presence of a large number of defects (marked by white circles) in the sample [35]. As shown in Fig. 1f and g, the octahedral 1 T phase and the trigonal prismatic 2 H phase structures can be observed. These results indicated that a 1 T/2 H mixed phase exist in C-MoS_2-Fe-x. However, no recognizable lattice of iron species was found in the images of HRTEM, probably attributed to the low amount of iron on the catalyst surface. HAADF-STEM was then performed to observe the dispersion of iron the catalyst of C-MoS_2-Fe-2 at the atomic scale. As displayed in Fig. S1a, the existence of atomic Fe (circled in red) was observed for C-MoS_2-Fe-2
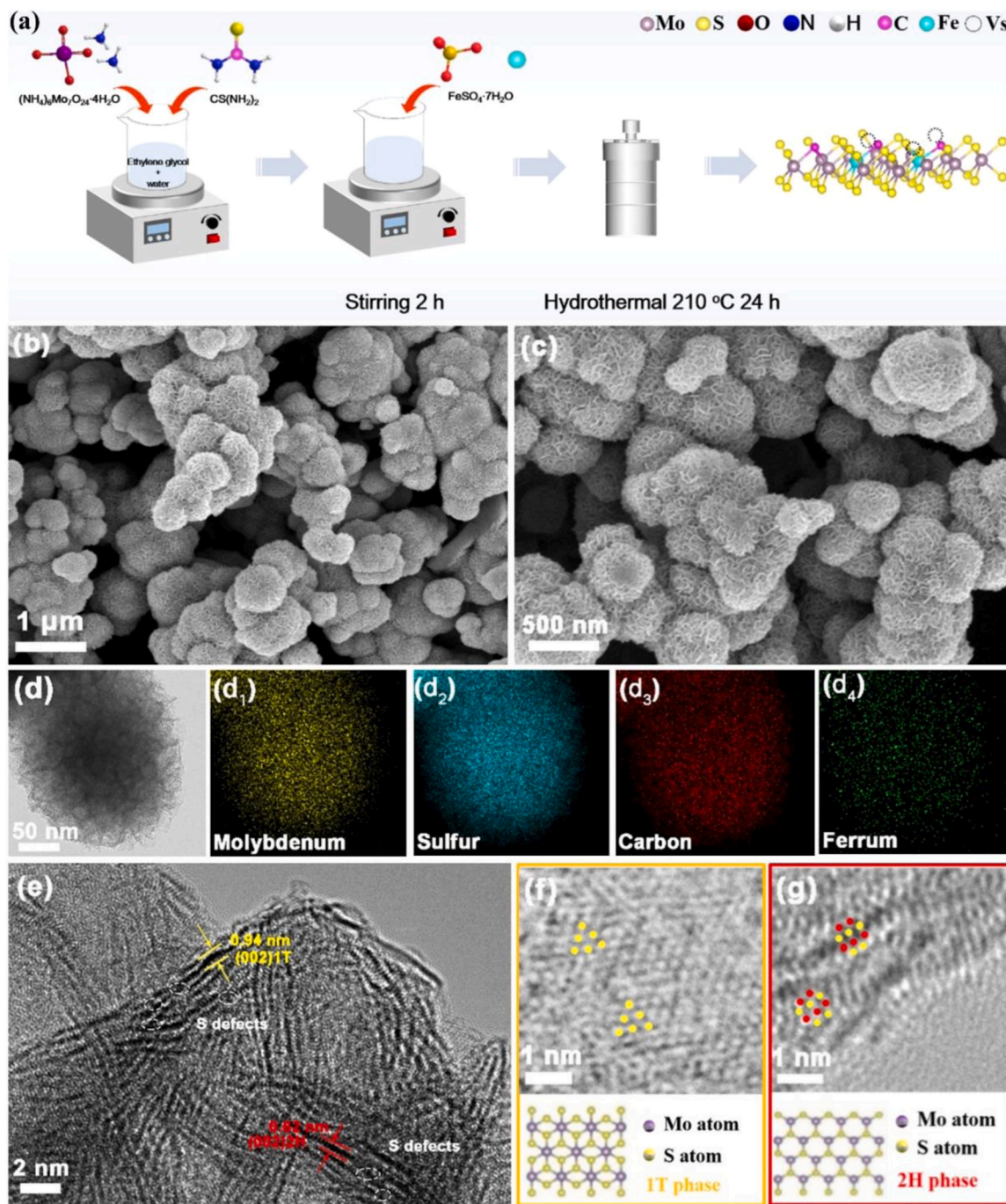
Fig. 1. Schematic illustration of the synthesis process (a). SEM images of C-MoS$_2$-Fe-2 (b, c). TEM image of C-MoS$_2$-Fe-2 (d), corresponding elemental mapping images (d$_1$-d$_4$). HRTEM images of C-MoS$_2$-Fe-2 (e, f, g).

sample.

XRD was used to study the crystallinity and structure of the samples. As displayed in Fig. 2a, pure MoS$_2$ showed three characteristic peaks at 14.3°, 33.2°, and 59.0°, corresponding to (002), (100), and (110) planes of 2 H phase MoS$_2$ (JCPDS: 37–1492) [36], respectively. Except for two similar peaks with MoS$_2$ at 33.2° and 59.0°, the new characteristic peaks at 9.0° as well as 17.2° corresponding to (002) and (004) in 1 T phase of C-MoS$_2$-2, indicating that this part may have been conversed to 1 T phase from 2 H phase [36]. Compared with MoS$_2$, MoS$_2$-Fe appeared new peaks at 37.0° and 56.7° that can be attributed to the typical peaks of FeS$_2$ [33]. However, in C-MoS$_2$-Fe-x all peaks related to FeS$_2$ almost disappear due to the decrease in crystallinity and the presence of the carbon layer on the surface [37]. Moreover, the characteristic peaks

were significantly broadened at 9.0°, 33.2°, and 59.0°, suggesting the 1 T/2 H mixed phase of MoS$_2$ and the low crystallinity due to defects, respectively [37,38].

Raman spectra was used to further explore the phase transformation. As illustrated in Fig. S2a, characteristic peaks corresponding to the E$_{1g}$ (280.0 cm^{-1}), E$_{2g}^1$ (376.0 cm^{-1}), and A$_{1g}$ (402.0 cm^{-1}) vibrations mode of 2 H phase MoS$_2$ were investigated for all samples [39]. Moreover, the E$_{2g}^1$ and A$_{1g}$ peaks of C-MoS$_2$-Fe-x were wider than those of MoS$_2$ and were slightly shifted, indicating the disordered structure in C-MoS$_2$-Fe-x [40,41]. Three typical peaks matching the J$_1$ (142.0 cm^{-1}), J$_2$ (225.0 cm^{-1}), and J$_3$ (335.0 cm^{-1}) vibrational modes of 1 T-phase MoS$_2$ were observed in C-MoS$_2$-Fe-x and C-MoS$_2$-2 compared to MoS$_2$ and MoS$_2$-Fe [33]. In summary, the introduction of carbon was the key factor
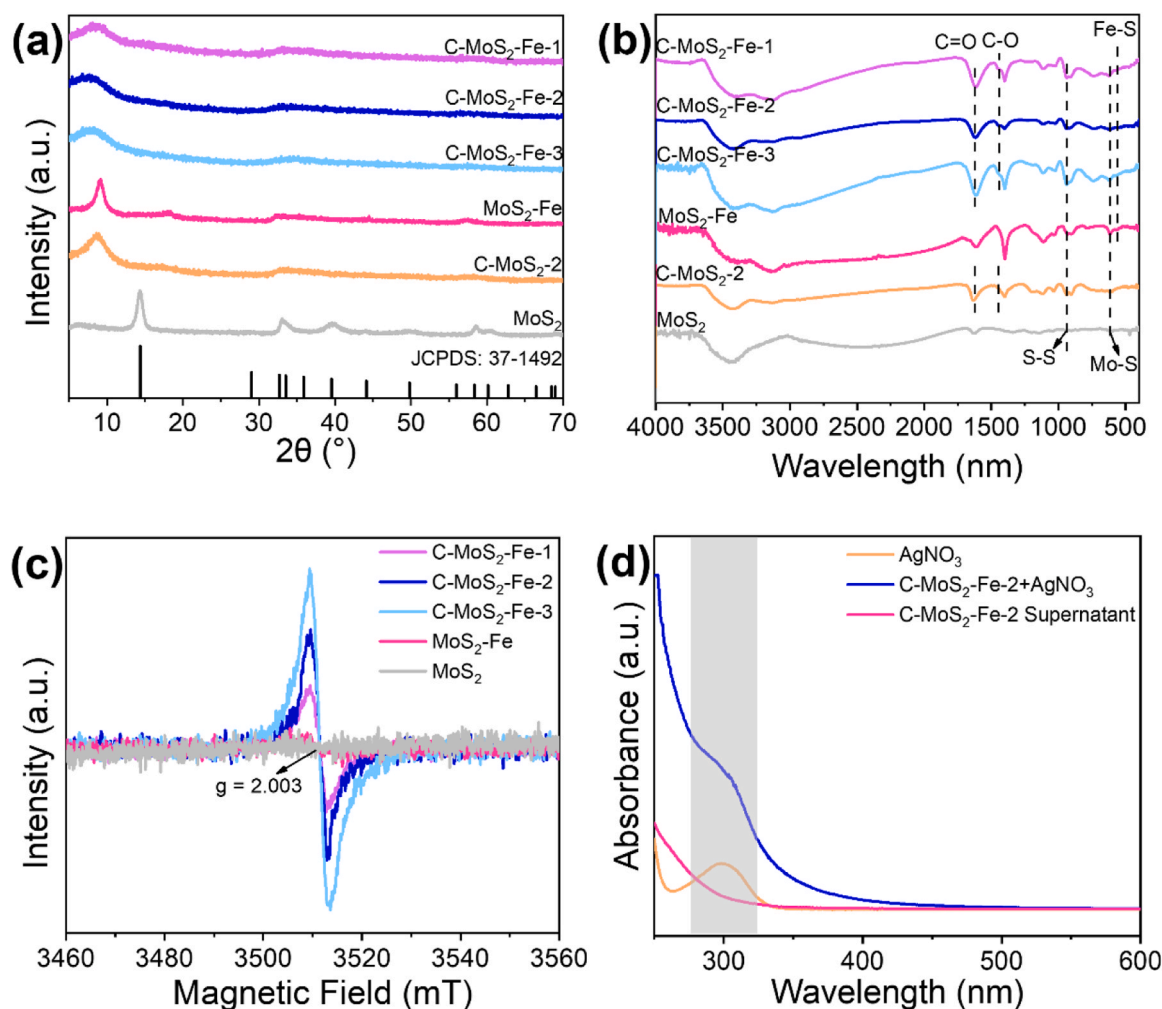
Fig. 2. XRD patterns (a), FT-IR spectra (b), and EPR spectra (c) of C-MoS$_2$-Fe-x, MoS$_2$-Fe, C-MoS$_2$-2, and MoS$_2$. UV–vis spectra of Ag$^+$ system, C-MoS$_2$-Fe-2 supernatant system, and C-MoS$_2$-Fe-2 +Ag$^+$ mixture system (d).

in promoting the transformation to the 1 T phase from the 2 H phase.

The functional groups in the samples were further monitored by FT-IR, as depicted in Fig. 2b. The peaks around 625 cm^{-1} and 940 cm^{-1} in all samples were related to the Mo-S and S-S stretching of MoS$_2$, respectively [41]. MoS$_2$-Fe showed a stretching vibrational peak around 561 cm^{-1}, which was related to the Fe–S form [33]. The same phenomenon occurred for C-MoS$_2$-Fe-x. Besides, abundant oxygenic functional groups such as C=O (1620 cm^{-1}) and C-O (1450 cm^{-1}) were observed in C-MoS$_2$-Fe-x and C-MoS$_2$-2 [42].

The porosity properties of different samples were analyzed by N$_2$ adsorption-desorption test (Fig. S2b, c). All the samples showed Type IV sorption isotherms with H3 hysteresis loops, suggesting that the samples had an unevenly distributed pore structure. The determined BET surface areas of MoS$_2$, MoS$_2$-Fe, C-MoS$_2$-Fe-1, C-MoS$_2$-Fe-2, and C-MoS$_2$-Fe-3 are 3.42, 5.98, 14.92, 18.90, and 10.83 m^2 g^{-1}, respectively; the pore sizes of samples between 2–4 nm. The incorporation of carbon resulted in a significant increase in the specific surface area of C-MoS$_2$-Fe-x.

The electronic structure of the catalysts was investigated by EPR spectroscopy. Generally, a stronger signal means more sulfur defects [43]. As illustrated in Fig. 2c, C-MoS$_2$-Fe-x showed a higher signal at g = 2.003 by comparison with MoS$_2$-Fe and MoS$_2$; furthermore, the intensity increased with the increase of ethylene glycol content, indicating that the introduction of carbon promotes the formation of S defects in C-MoS$_2$-Fe-x. Defects favored the electron transfer and thus enhanced the catalytic performance of C-MoS$_2$-Fe-x. Besides, the existence of sulfur defect was conducive to reducing the energy difference between

the 1 T phase and the 2 H phase and made the 1 T phase exist stably [44, 45].

The unsaturated S atoms on the catalyst could be captured to create H$_2$S, which would react with Ag$^+$ from AgNO$_3$ to generate Ag$_2$S, so Ag$_2$S could be used to confirm the presence of S defects [46]. C-MoS$_2$-Fe-2 was used as a representative catalyst for the experiments. As displayed in Fig. 2d, the C-MoS$_2$-Fe-2 + AgNO$_3$ system exhibited an absorption peak at 310 nm similar to that of the AgNO$_3$ system, which corresponds to the typical peak of Ag$_2$S [47]. This suggests that there was a lot of unsaturated sulfur on the surface of C-MoS$_2$-Fe-2, and the Mo^{4+} active sites thus exposed were favorable for the reduction of Fe^{3+}.

XPS was used to analyze the chemical components and valence states of the different sample's surface. In the Mo 3d XPS spectra (Fig. 3a), the characteristic peaks at 228.5 eV and 231.7 eV corresponded to Mo^{4+} 3d$_{5/2}$ and Mo^{4+} 3d$_{3/2}$ in 1 T phase MoS$_2$, respectively; the characteristic peaks at 228.9 eV and 232.7 eV corresponded to Mo^{4+} 3d$_{5/2}$ and Mo^{4+} 3d$_{3/2}$ in 2 H phase MoS$_2$, respectively [45]. The characteristic peak at 225.9 eV was attributed to S 2 s [40]. Compared to pure MoS$_2$, the peaks of the 2 H phase Mo 3d$_{5/2}$ and Mo 3d$_{3/2}$ in the C-MoS$_2$-Fe-x were shifted towards a lower binding energy region, which may be due to the doping of carbon. The characteristic peak at 235.8 eV was ascribed to Mo^{6+} [48]. Then, the 1 T phase proportion in the C-MoS$_2$-Fe-x was calculated (Table S1), which was about 57.5% (C-MoS$_2$-Fe-1), 65.2% (C-MoS$_2$-Fe-2), and 63.9% (C-MoS$_2$-Fe-3). The introduction of carbon induced the glide of S atomic planes around the carbon-incorporated area, favoring the transition of the 2 H phase to the 1 T phase in MoS$_2$
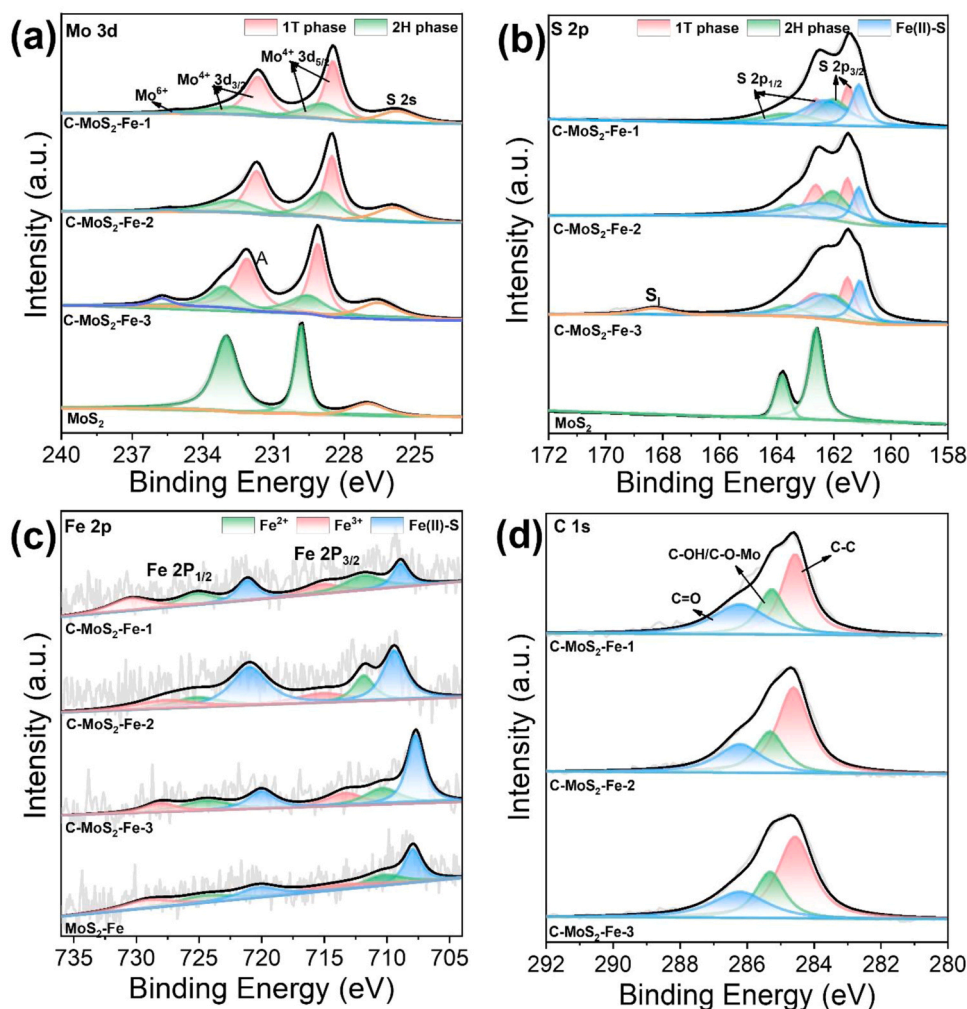
Fig. 3. High-resolution XPS spectra of Mo 3d (a), S 2p (b), Fe 2p (c), and C 1 s (d) region of different samples.

[23]. However, doping too much C could result in the 1 T phase proportion decline. The S 2p region (Fig. 3b) of C-MoS$_2$-Fe-x presented the peaks at 162.0 eV and 163.6 eV for 2 H phase MoS$_2$ [45]; in addition, two new peaks appeared at 161.5 and 162.7 eV, corresponding to S 2p$_{3/2}$ and S 2p$_{1/2}$ in 1 T phase MoS$_2$ [47,49]. Similarly, the peaks of the 2 H phase S 2p$_{3/2}$ and S 2p$_{1/2}$ orbitals in the C-MoS$_2$-Fe-x were also shifted towards a lower binding energy region compared to pure MoS$_2$, which could be due to the introduction of carbon. Peaks near 168.9 eV in C-MoS$_2$-Fe-3 were S$_I$ (-SOn-), indicating that part of the S element on the MoS$_2$ surface was oxidized [50]. For the Fe 2p spectrum (Fig. 3c), the peaks at 710.3, 724.5, 713.8 and 727.1 eV corresponded to Fe^{2+} 2p$_{3/2}$, Fe^{2+} 2p$_{1/2}$, Fe^{3+} 2p$_{3/2}$ and Fe^{3+} 2p$_{1/2}$, respectively [51]. The peaks at 707.7 and 720.2 eV belonged to Fe(II)-S [47]; while in the S 2p spectrum, the peaks located at 162.3 and 161.1 eV confirm the Fe(II)-S presence as well [51]. As shown in Fig. 3d, the peaks at 284.6 eV and 286.2 eV correspond to C-C and C=O, respectively. Moreover, the characteristic peak at 285.3 eV corresponds to C-OH/C-O-Mo, suggesting the doping of C into MoS$_2$, leading to some defects [37]. Meanwhile, the atomic ratio of S: Mo (Table S2) in catalysts was about 1.78: 1 (C-MoS$_2$-Fe-1), 1.70: 1 (C-MoS$_2$-Fe-2), and 1.65: 1 (C-MoS$_2$-Fe-3). All were lower compared to 1.82: 1 of MoS$_2$-Fe, suggesting that defects were ascribed to S vacancies (SVs). This was in agreement with the findings from the EPR spectrum. Table S3 illustrated the average valence of Mo in samples. C-MoS$_2$-Fe had a lower average valence of Mo (4.02) than that of MoS$_2$-Fe (4.1). This result indicated that the defect created by the introduction of C allowed more electrons to be localized to the Mo site.

Thus, more Fe^{3+} can be reduced through the electron-rich Mo sites from the defective C-MoS$_2$-Fe to activate PMS.

3.2. Simultaneous removal ENR and Cr(VI) using C-MoS$_2$-Fe-x

The ability of C-MoS$_2$-Fe-x activated PMS was studied systematically by simultaneous removal ENR and Cr(VI). The adsorption experiment was first performed. The concentrations of ENR (Fig. S3a) and Cr(VI) (Fig. S3b) were almost unchanged after 30 min, indicating that the solution reached the adsorption equilibrium. As exhibited in Fig. 4a and b, the removal rate of ENR was only 10.0% (30 min) with only PMS, while the concentration of Cr(VI) was hardly reduced. What's more, the C-MoS$_2$-Fe-x/PMS system showed excellent performance, which was significantly better than those of MoS$_2$-Fe/PMS, C-MoS$_2$-2/PMS, and MoS$_2$/PMS systems. Three C-MoS$_2$-Fe-x samples follow the removal efficiency order of C-MoS$_2$-Fe-1 < C-MoS$_2$-Fe-3 < C-MoS$_2$-Fe-2. In particular, C-MoS$_2$-Fe-2 exhibited great removal efficiencies of ENR (100.0%) and Cr(VI) (96.0%) in 30 min via activating PMS. As shown in Figs. 4c, 4d, S4a, and S4b, the reaction rate constant of ENR removal in C-MoS$_2$-Fe-2/PMS (k = 0.200 min^{-1}) is around 15.4 times as high as that of MoS$_2$-Fe/PMS (k = 0.013 min^{-1}), 25.0 times as high as that of C-MoS$_2$-2/PMS (k = 0.008 min^{-1}), and even 40 times as high as the MoS$_2$/PMS system (k = 0.005 min^{-1}); meanwhile, the removal rate constant of Cr(VI) in the C-MoS$_2$-Fe-2/PMS (k = 0.110 min^{-1}) is around 8.5 times as high as the MoS$_2$-Fe/PMS (k = 0.013 min^{-1}), 12.2 times as high as the C-MoS$_2$-2/PMS (k = 0.009 min^{-1}), and 27.5 times as high as the MoS$_2$/
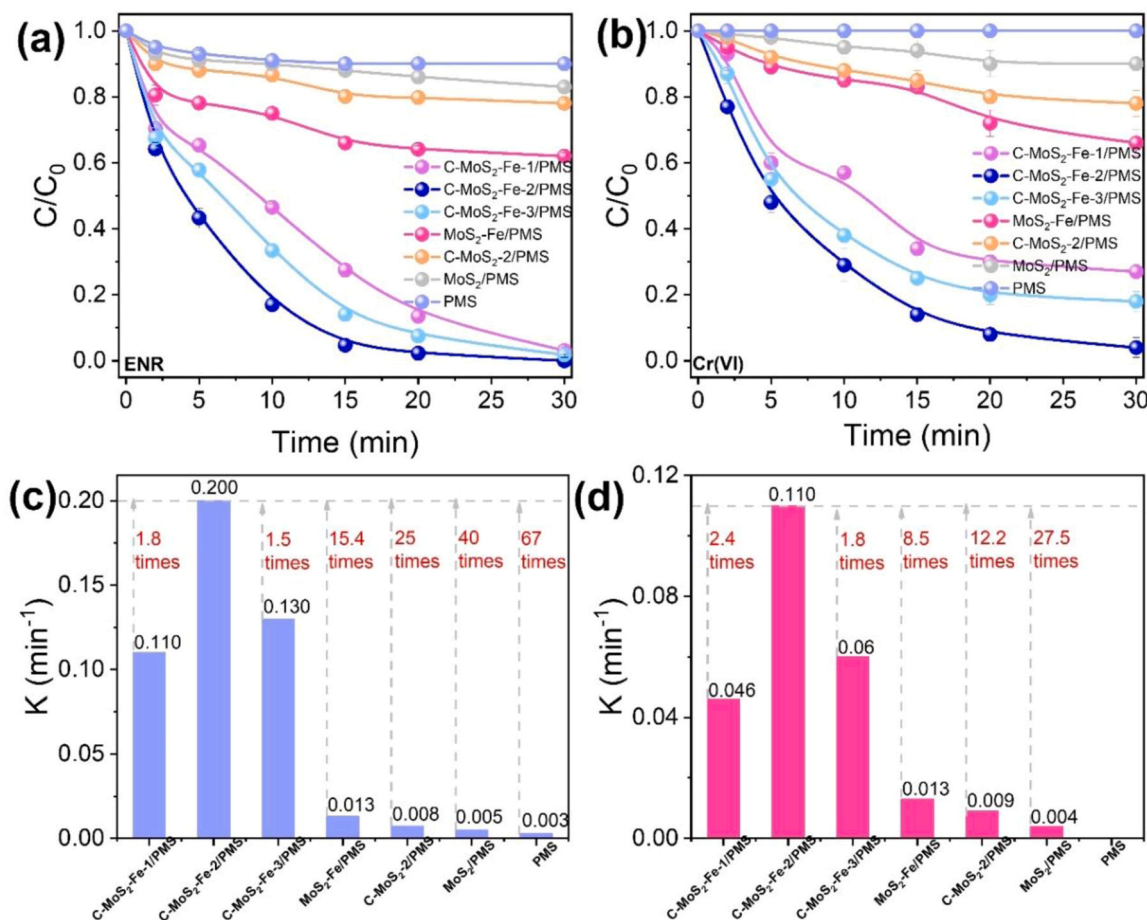
Fig. 4. The removal efficiency and kinetic rate constants under the co-existence of ENR (a, c) and Cr(VI) (b, d) by different systems. (General condition: [catalyst] = 0.2 g L^{-1}, [PMS]$_0$ = 0.2 mM, [ENR]$_0$ = 10 mg L^{-1}, [Cr(VI)]$_0$ = 5 mg L^{-1}, pH 3).

PMS system (k = 0.004 min^{-1}). C-MoS$_2$-Fe-x had more active sites and exposed more Mo^{4+} by incorporating of carbon, benefitting the conversion of Fe^{3+} to Fe^{2+}. The reaction rate constant for pollutant removal by C-MoS$_2$-Fe-3 as the catalyst (k = 0.130 min^{-1}) reduced compared with that of C-MoS$_2$-Fe-2, which was possibly due to the excess S defects leading to the leaching of excessive molybdenum ions from the inner of the catalyst, disrupting the catalyst structure and affecting the catalytic activity. Accordingly, C-MoS$_2$-Fe-2 with the highest reaction rate and great physicochemical properties was used as a catalyst for the following experiments.

Fig. S5 and S6 showed the effects of the catalyst dosage, PMS concentrations, pollutant concentrations, and pH value on the removal of ENR and Cr(VI). The reaction rate constant was enhanced with increasing amounts of catalyst (Fig. S5a, S5a', S6a, and S6a') and PMS concentrations (Fig. S5b, S5b', S6b, and S6b'). This may be due to the increase in active sites involved in the reaction, which benefited the generation of reactive oxygen species [52]. However, with further increasing their concentration or quantity, the corresponding removal rate constants increased insignificantly. These suggested that 0.2 g L^{-1} of C-MoS$_2$-Fe-2 was enough to activate PMS (0.2 mM) for pollutant removal. Fig. S5c, S5c', S6c, and S6c' showed that the system could achieve removal efficiently at different pollutant concentrations, suggesting that it has a great organic pollutant removal ability. As shown in Fig. S5d, S5d', S6d, and S6d', when the pH value is 2–8, the ENR removal efficiency was all above 94.0% (30 min). Acidic conditions favoured the maintenance of Fe^{2+} state and improved catalytic properties [52]. Besides, PMS could operate over a wide pH range (2−8), which was because SO$_4^{\bullet-}$ could produce other reactive oxygen species under weakly alkaline conditions (Eqs. 1 and 2) [38,53]. In addition, Cr

(VI) was effectively removed at pH 2–3 (> 96.0%, k > 0.11 min^{-1}); as the pH continued to increase to 4 and 6, the removal rate constants decreased significantly (k = 0.05 and 0.04 min^{-1}, respectively), and a further increase in pH to 8 led to a further decrease in the removal rate. Cr(VI) exists in the form of CrO$_4^{2-}$ and HCrO$_4^-$ under acidic and alkaline conditions, respectively. In acidic conditions, the reduction of the HCrO$_4^-$ ion is facilitated by an excess hydrogen ion (H$^+$); however, in alkaline conditions, the reduction of the CrO$_4^{2-}$ ion is difficult to carry out due to the presence of large amounts of hydroxide ions (OH$^-$), and the corresponding reaction process (Eqs. 3 and 4) [54]. Cr(III) reduced from Cr(VI) can form a precipitate under alkaline conditions and cover the active site of the catalyst, thereby reducing the Cr(VI) removal efficiency. Therefore, pH 3 was chosen as the appropriate pH.

$$SO_4^{\bullet-} + H_2O \rightarrow SO_4^{2-} + \bullet OH + H^+ \tag{1}$$

$$SO_4^{\bullet-} + OH^- \rightarrow SO_4^{2-} + \bullet OH \tag{2}$$

$$HCrO_4^- + 7\,H^+ + 3e^- \rightarrow Cr^{3+} + 4\,H_2O \tag{3}$$

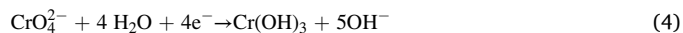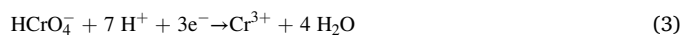$$CrO_4^{2-} + 4\,H_2O + 4e^- \rightarrow Cr(OH)_3 + 5OH^- \tag{4}$$

Table S4 demonstrated the effectiveness of various catalysts activated PMS for organic pollutants and Cr(VI) removal to evaluate the effectiveness of C-MoS$_2$-Fe-2. These results show that C-MoS$_2$-Fe-2 with the quickest reaction rate and best removal efficiency performs the best in comparison with other reports.

3.3. Insight into the reaction mechanism

In general, the electrochemical properties of the material are positively correlated with the ability of advanced oxidation reactions [39, 55]. The electrochemical properties of the catalysts were investigated using electrochemical impedance spectroscopy (EIS) (Fig. S7). The charge transfer resistance of the C-MoS$_2$-Fe-x became smaller compared to that of MoS$_2$-Fe, suggesting that the carbon-doped structure brings better charge transfer capability. Among all C-MoS$_2$-Fe-x samples, C-MoS$_2$-Fe-2 showed the smallest interfacial charge transfer resistance, indicating the strongest electron transfer capability. This was attributed to the fact that the 1 T phase of MoS$_2$ was highly electrochemically active, and C-MoS$_2$-Fe-2 contained the largest proportion of the 1 T phase.

Based on the analysis of physicochemical properties, structural models of MoS$_2$-Fe (Fig. 5a) and C-MoS$_2$-Fe were constructed (Fig. 5b). The main effect of C incorporation was to transform the 2 H phase MoS$_2$ to the 1 T phase as well as the introduction of an abundance of defects. The increase in the content of the 1 T phase and the abundance of defects improved the conductivity and the electron density of the C-MoS$_2$-Fe respectively, thereby increasing the electron transfer rate. To further confirm the above conclusions, DFT calculations were performed. The calculated DOS (Fig. 5c and d) showed that C-MoS$_2$-Fe has a narrower band gap (about 0.3 eV smaller) than MoS$_2$-Fe, which may be due to the energy level change caused by C introduction. In addition, the introduction of carbon atoms had a remarkable effect on increasing the charge density (Fig. 5f) compared to MoS$_2$-Fe (Fig. 5e). S defect contributed to the formation of electron deficient centers, leading to a potential shift of charge transfer to Mo atoms [56]. This result was in agreement with the XPS results of increasing electron density around Mo and lower average valence of Mo in defective C-MoS$_2$-Fe. The above results indicated that C-MoS$_2$-Fe possessed superior electron transfer capability and promoted the reaction kinetics.

It has been widely observed that defects can not only change the surface charge distribution but also have an effect on the adsorption energy [57]. To further determine the mechanism by which S defects promote catalytic performance, the PMS adsorption energies on MoS$_2$-Fe and C-MoS$_2$-Fe were determined by first-principles DFT calculations. Fig. 5g and h showed the MoS$_2$-Fe and C-MoS$_2$-Fe models after the adsorption of PMS. To the best of our knowledge, the PMS adsorption energy (E$_{ads}$) is an important criterion for assessing the decomposition of PMS [58]. The lower the PMS adsorption energy is, the easier the PMS adsorption on the catalyst is [59]. The calculated adsorption energies of PMS on MoS$_2$-Fe and C-MoS$_2$-Fe − 0.5726 and − 1.1353 eV, respectively, suggesting that adsorption of PMS on C-MoS$_2$-Fe was more beneficial as compared to that on MoS$_2$-Fe, which facilitated the reaction of PMS with C-MoS$_2$-Fe.

The results of EIS and DFT calculations demonstrated that the introduction of the 1 T phase and the abundance of S defects in C-MoS$_2$-Fe-2 improved the performance of the activated PMS.

Free radical capture and EPR experiments were conducted to determine the active components in C-MoS$_2$-Fe-2/PMS at the co-existence of ENR and Cr(VI). Particularly, MA (for •OH and SO$_4^{•-}$ with k = 9.7 × 10^9 M^{-1} s^{-1} and 1.1 × 10^7 M^{-1} s^{-1}, respectively), TBA (for •OH with k = 3.8–7.6 × 10^8 M^{-1} s^{-1}), BQ (for •O$_2^-$ with k = 5 × 10^7 M^{-1} s^{-1}), FFA (for ^{1}O$_2$ with k = 1.2 × 10^8 M^{-1} s^{-1}), PTL (for Fe^{2+}), and KBrO$_3$ (for e$^-$) [39,60] were added as quenching agents into the C-MoS$_2$-Fe/PMS system, and for comparison, active components in MoS$_2$-Fe/PMS system were also identified.

Firstly, as shown in Fig. S8a, b, and c, after the addition of PMSO, there was no significant change in the removal of ENR and Cr(VI), and there was no production of PMSO$_2$. This indicated that the pollutants were not removed by the oxidation process of high valence metals. As illustrated in Fig. S8d, the removal efficiency of ENR decreased with the addition of MA, FFA, TBA, and BQ, indicating the involvement of •OH, ^{1}O$_2$, as well as •O$_2^-$ in the removal of ENR in MoS$_2$-Fe/PMS. The

efficiency of ENR removal decreased significantly with the addition of FFA (Fig. 6a), suggesting that ^{1}O$_2$ accounted for the removal of ENR in the C-MoS$_2$-Fe-2/PMS. Meanwhile, in both systems (Fig. S8e and Fig. 6b), the removal of Cr(VI) almost did not change after adding MA, FFA, TBA, and BQ, while the removal efficiency decreased with the addition of PTL and KBrO$_3$. The oxidation potential of Cr$_2$O$_7^{2-}$/Cr^{3+} is 1.35 V, whereas Fe^{3+}/Fe^{2+} has an oxidation potential of 0.77 V and Mo^{6+}/Mo^{4+} has an oxidation potential of 0.11 V. Therefore, thermodynamically Fe^{2+} preferentially reduced Cr(VI) to Cr(III). These results indicated that the Fe^{2+} and e$^-$ accounted for Cr(VI) reduction in both systems. However, there was a difference in the active components for ENR removal between MoS$_2$-Fe/PMS and C-MoS$_2$-Fe-2/PMS systems.

In order to further determine the active fractions produced for ENR removal in the systems, EPR tests were conducted. As shown in Fig. 6c, stronger signals with an intensity ratio of 1:2:2:1 occurred in C-MoS$_2$-Fe-2/PMS than in other two systems, corresponding to the DMPO-•OH adducts along with DMPO-SO$_4^{•-}$ adducts [61], but the intensities of DMPO-SO$_4^{•-}$ adducts peaks was insignificant. In addition, weak signals of DMPO− •O$_2^-$ adducts were detected in the three systems (Fig. 6d). The •O$_2^-$ in the PMS system was probably obtained by •OH conversion [62,63]. As presented in Fig. 6e, the characteristic signal of TEMP-^{1}O$_2$ adducts with an intensity ratio of 1:1:1 was much higher in C-MoS$_2$-Fe-2/PMS than in other two systems, suggesting a higher amount of ^{1}O$_2$ was generated in C-MoS$_2$-Fe-2/PMS. Furthermore, the concentration of various active fractions involved in ENR removal was quantified by the steady-state concentrations method using BA, NB, NBT, and FFA as the probe compounds. As displayed in Fig. 6f, the steady-state concentration of ^{1}O$_2$, •OH, •O$_2^-$, as well as SO$_4^{•-}$ for C-MoS$_2$-Fe-2/PMS was calculated as 1.28 × 10^{-10}, 5.13 × 10^{-13}, 3.60 × 10^{-13}, and 1.07 × 10^{-15} M according to the formulas presented in Text S6, which was 1.60, 3.05, 1.00, and, 6.3 times than that of ^{1}O$_2$ (8.00 × 10^{-11} M), •OH (1.68 × 10^{-13} M), •O$_2^-$ (3.46 × 10^{-13} M), and SO$_4^{•-}$ (1.75 × 10^{-16} M) in MoS$_2$-Fe/PMS system, respectively. These results were in good agreement with that of quenching and EPR experiments. The highest ^{1}O$_2$ concentration in C-MoS$_2$-Fe-2/PMS illustrated that ^{1}O$_2$ was the predominant active component in ENR removal. It suggested that the great increase in ^{1}O$_2$ generation in C-MoS$_2$-Fe-2/PMS significantly improved pollutants removal efficiency. In addition, the PMS decomposition rates in systems were tested (Fig. S8f). The decomposition efficiency of PMS was 71.5% in MoS$_2$-Fe/PMS, while the C-MoS$_2$-Fe-2/PMS could reach 98.0%. It is also confirmed that C-MoS$_2$-Fe-2 played an important role in promoting the activation of PMS.

In order to further reveal the mechanism of ENR and Cr(VI) removal by C-MoS$_2$-Fe-2 activated PMS, the XPS of Fe 2p (Fig. 7a) and Mo 3d (Fig. 7b) of C-MoS$_2$-Fe-2 for different reaction times reaction were investigated, and more information was shown in Table S5. With reaction time increased (Fig. 7c and d), the Fe^{2+} content decreased from 75.5% (Before the reaction) to 49.0% (15 min) and then increased to 54% (30 min), while at the same time, the Fe^{3+} content increased from 25.5% (Before the reaction) to 51.0% (15 min) and then decreased to 46.0% (30 min). The content of Mo^{4+} dropped by 4.7% after the reaction, suggesting that Fe^{3+} was reduced to Fe^{2+} by Mo^{4+} and achieved its self-Fe^{3+}/Fe^{2+} cycling, thus maintaining the high catalytic activity. Fig. 7e and f illustrated the XPS spectra of Cr 2p and C 1 s of the catalyst after the reaction. The characteristic peaks at 576.7 eV and 586.5 eV, correspond to Cr 2p$_{3/2}$ and Cr 2p$_{1/2}$, respectively, indicating the conversion of Cr(VI) to Cr(III) [64]. The C═O content of the C-MoS$_2$-Fe-2 decreased from 23.5% to 21.0%. The results indicate that a small amount of C═O can promote electron transfer as well as react with PMS to form ^{1}O$_2$ [65]. Moreover, the S 2p XPS spectra of the catalyst after the reaction was tested (Fig. S9). The decrease in the amount of the low valence sulfur from 100.0% to 95.0%, was attributed to the transfer of electrons from low-valent S to Fe^{3+}.

According to the above works, the possible mechanism for the removal of ENR and Cr(VI) by the C-MoS$_2$-Fe-2/PMS system was proposed (Scheme 1), which was divided into two parts: oxidative
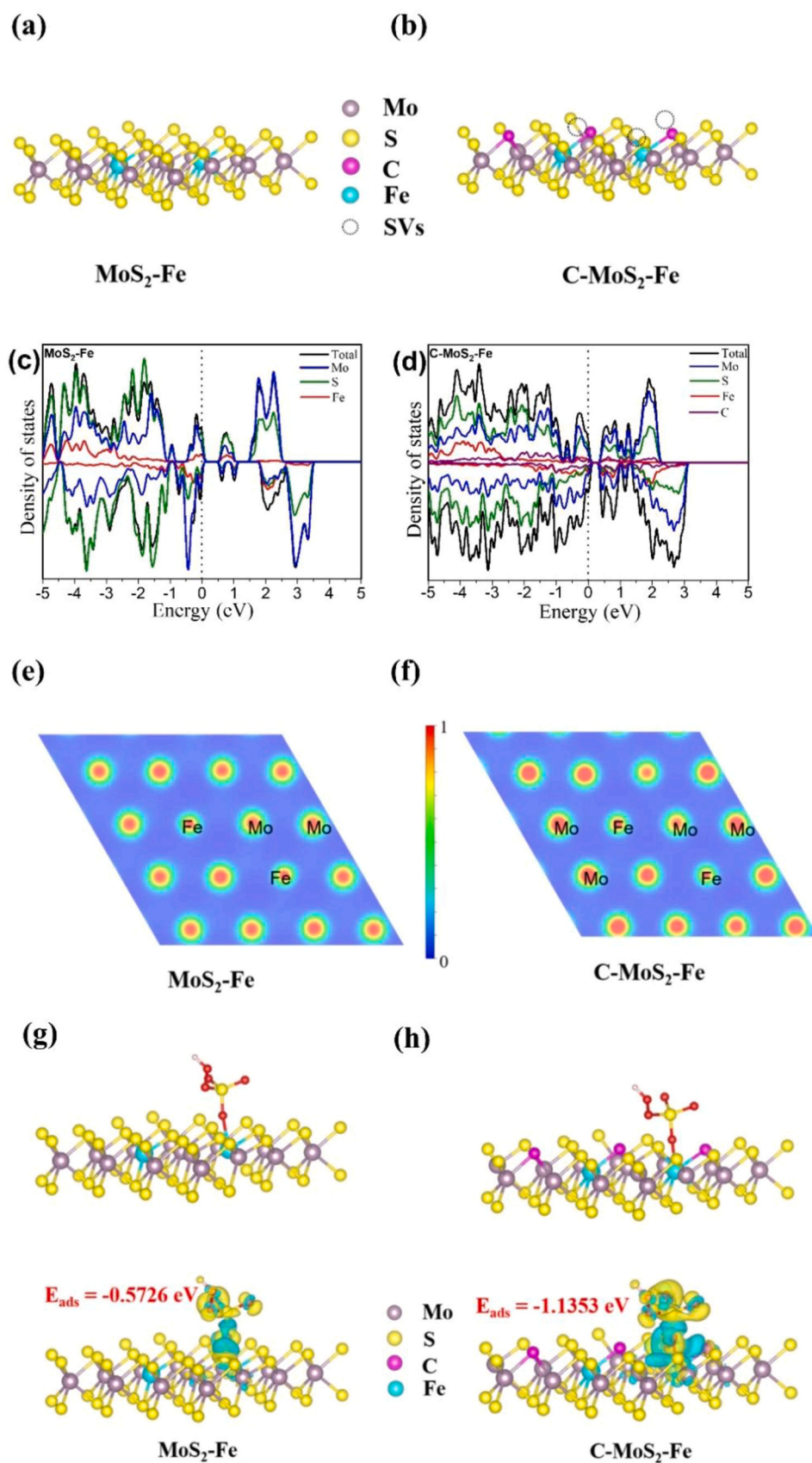
Fig. 5. Calculated DOS (c, d) and the charge density distributions (e, f) of MoS$_2$-Fe and C-MoS$_2$-Fe-x based on the optimized structure models (a, b). PMS adsorption configuration and energy of PMS on MoS$_2$-Fe (g) and C-MoS$_2$-Fe (h).

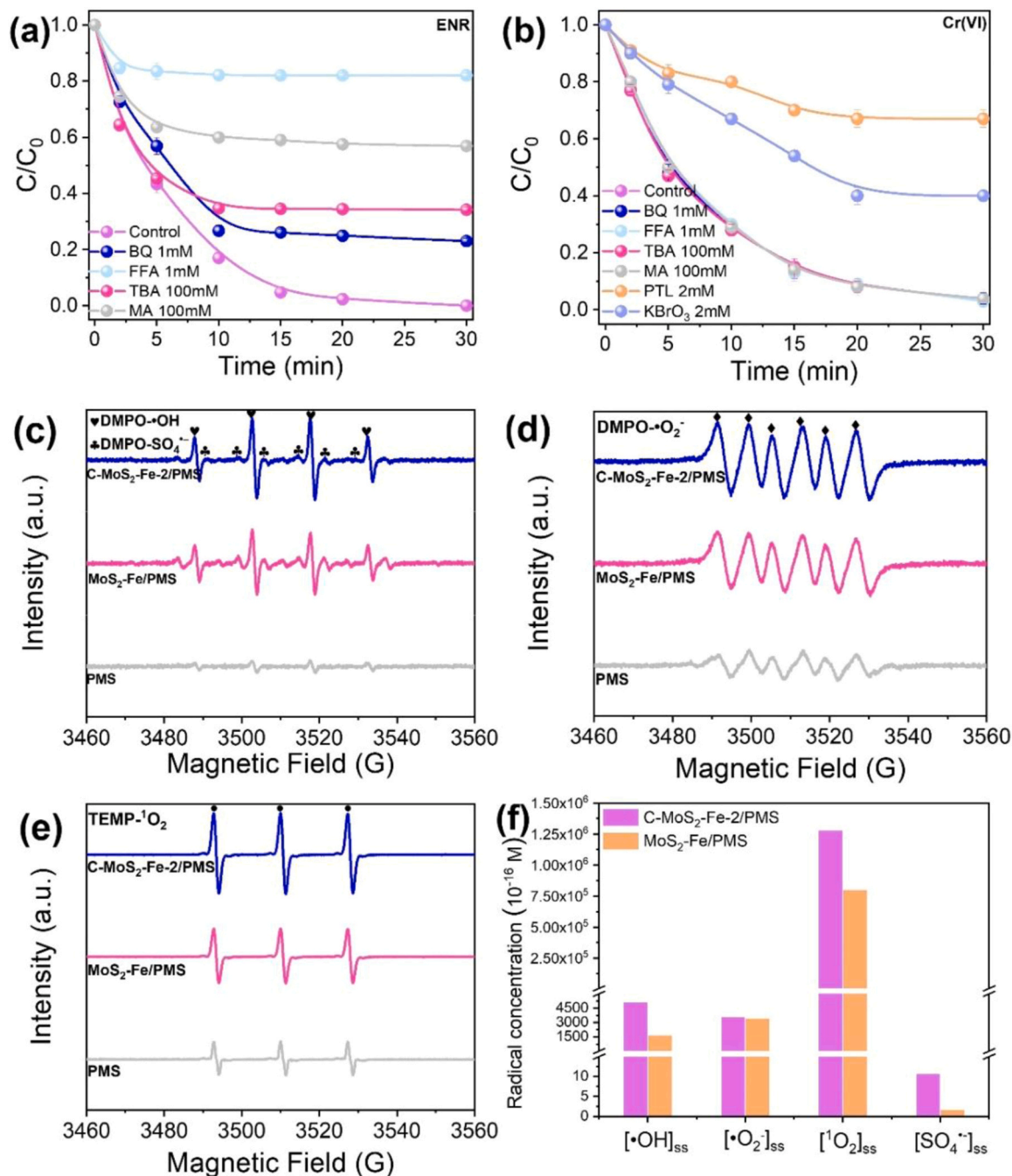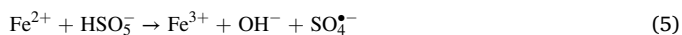**Fig. 6.** Quenching tests of C-MoS$_2$-Fe-2/PMS system (a, b). (Reaction condition: [catalyst] =0.2 g L^{-1}, [PMS]$_0$ = 0.2 mM, [ENR]$_0$ = 10 mg L^{-1}, [Cr(VI)]$_0$ = 5 mg L^{-1}, [BQ]$_0$ = 1 mM, [FFA]$_0$ = 1 mM, [TBA]$_0$ = 100 mM, [MA]$_0$ = 100 mM, [PTL]$_0$ = 2 mM, [KBrO$_3$]$_0$ = 2 mM, pH 3). EPR spectra with DMPO (c, d) and TEMP (e) as spin-trapping agents in C-MoS$_2$-Fe-2/PMS, MoS$_2$-Fe/PMS, and PMS systems. The steady-state concentrations of •OH, •O$_2^-$, ^{1}O$_2$ and SO$_4^{•-}$ in C-MoS$_2$-Fe-2/PMS and MoS$_2$-Fe/PMS systems (f).

degradation of ENR and reduction of Cr(VI). On the one hand, possible processes for oxidative degradation of ENR were as follows: Firstly, Fe^{2+} in the catalyst activated PMS, generating •OH and SO$_4^{•-}$ and forming Fe^{3+} (Eqs. 5 and 6). Activated PMS can produce a small amount of H$_2$O$_2$ in water, which rapidly reacted with •OH to form •O$_2$H, and then rapidly converted to •O$_2^-$ (Eq. 7−9) [66]. The generated Fe^{3+} was reduced to Fe^{2+} by Mo^{4+} in the catalyst (Eq. 10). Mo^{6+} further reacted with HSO$_5^-$ and was reduced to Mo^{4+} and produced SO$_5^{•-}$ (Eq. 11) [67]. Thus, the C-MoS$_2$-Fe-2 catalyst realized its own redox cycle of Fe^{2+}/Fe^{3+} and Mo^{4+}/Mo^{6+}, ensuring a large amount of active sites involved in the reaction process. In addition, ^{1}O$_2$ was further produced as Eqs. 12–14

[68]. Secondly, the C═O of C-MoS$_2$-Fe-2 can be used as the active sites to directly decompose PMS to the production of ^{1}O$_2$ (Eq. 15) [69–71].- At last, the presence of SVs also contributed to the production of ^{1}O$_2$ (Eq. 16) [72]. ENR was effectively degraded to smaller molecules (Eq. 17).

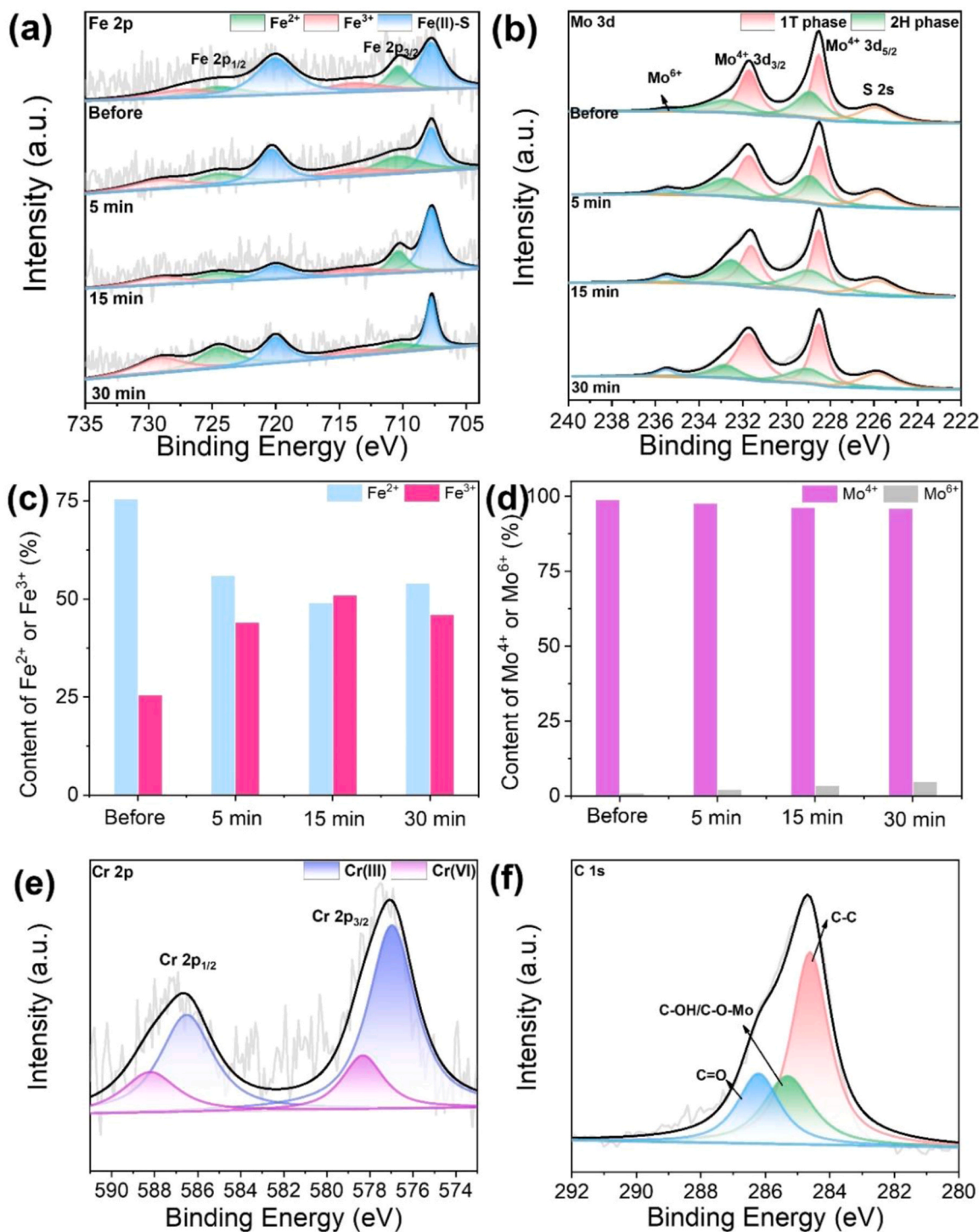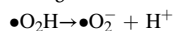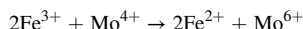$$Fe^{2+} + HSO_5^- \rightarrow Fe^{3+} + OH^- + SO_4^{•-} \tag{5}$$

$$Fe^{2+} + HSO_5^- \rightarrow Fe^{3+} + SO_4^{2-} + •OH \tag{6}$$

$$H_2O + HSO_5^- \rightarrow H_2O_2 + HSO_4^- \tag{7}$$

$$•OH + H_2O_2 \rightarrow •O_2H + H_2O \tag{8}$$

Fig. 7. XPS spectra of Fe 2p (a) and Mo 3d (b) of C-MoS$_2$-Fe-2 during the reaction. Corresponding content of Fe^{2+}/Fe^{3+} (c) and Mo^{4+}/Mo^{6+} (d) of C-MoS$_2$-Fe-2 during the reaction. XPS spectra of Cr 2p (e), and C 1 s (f) of C-MoS$_2$-Fe-2 after the reaction.

$$\bullet O_2H \rightarrow \bullet O_2^- + H^+ \tag{9}$$

$$2Fe^{3+} + Mo^{4+} \rightarrow 2Fe^{2+} + Mo^{6+} \tag{10}$$

$$Mo^{6+} + 2HSO_5^- \rightarrow 2SO_5^{\bullet-} + Mo^{4+} + 2\ H^+ \tag{11}$$

$$Fe^{3+} + HSO_5^- \rightarrow Fe^{2+} + SO_5^{\bullet-} + H^+ \tag{12}$$

$$SO_5^{\bullet-} + SO_5^{\bullet-} \rightarrow 2SO_4^{2-} + {}^1O_2 \tag{13}$$

$$SO_5^{2-} + HSO_5^- \rightarrow HSO_4^- + SO_4^{2-} + {}^1O_2 \tag{14}$$

$$C{=}O + 2HSO_5^- \rightarrow 2SO_4^{2-} + 2\ H^+ + {}^1O_2 \tag{15}$$

$$SVs + 2HSO_5^- \rightarrow 2HSO_4^- + {}^1O_2 \tag{16}$$
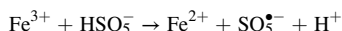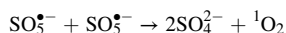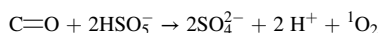
$${}^1O_2/SO_4^{\bullet-}/\bullet OH/\bullet O_2^- + ENR \rightarrow \text{Degradation products} \tag{17}$$

On the other hand, the possible mechanisms of Cr(VI) reduction were as follows. Cr(VI) was adsorbed onto the surface of C-MoS$_2$-Fe-2, which was then reduced to Cr(III) by Fe^{2+} in the catalyst (Eq. 18); meanwhile, the C-MoS$_2$-Fe-2 catalyst carried out its own Fe^{2+}/Fe^{3+} and Mo^{4+}/Mo^{6+} redox cycling, which continually provided active sites to participate in

Scheme 1. Proposed mechanism in C-MoS$_2$-Fe/PMS system.

the reaction (Eqs. 10 and 11). In addition, the electrons present in the system can also reduce Cr(VI) (Eq. 19) [39].

$$3Fe^{2+} + Cr(VI) \rightarrow 3Fe^{3+} + Cr(III) \tag{18}$$

$$3e^- + Cr(VI) \rightarrow Cr(III) \tag{19}$$

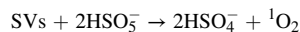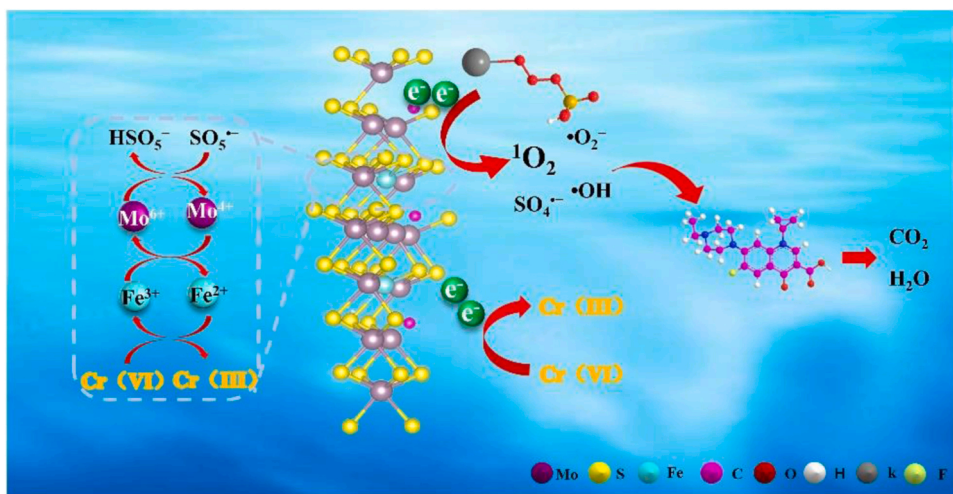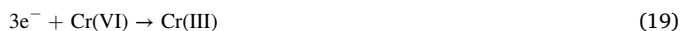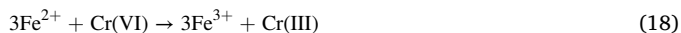Additionally, the synergistic removal of ENR and Cr(VI) was investigated and the results were displayed in Fig. 8. As the concentration of Cr(VI) was increased from 2.5 mg L^{-1} to 20 mg L^{-1}, the removal rate of ENR was consistently maintained at 100% (Fig. 8a) with no significant change in the reaction rate constant (Fig. 8c). This indicated that the addition of metal ions had little effect on the removal of ENR. However, with the increase of ENR concentration, although the removal
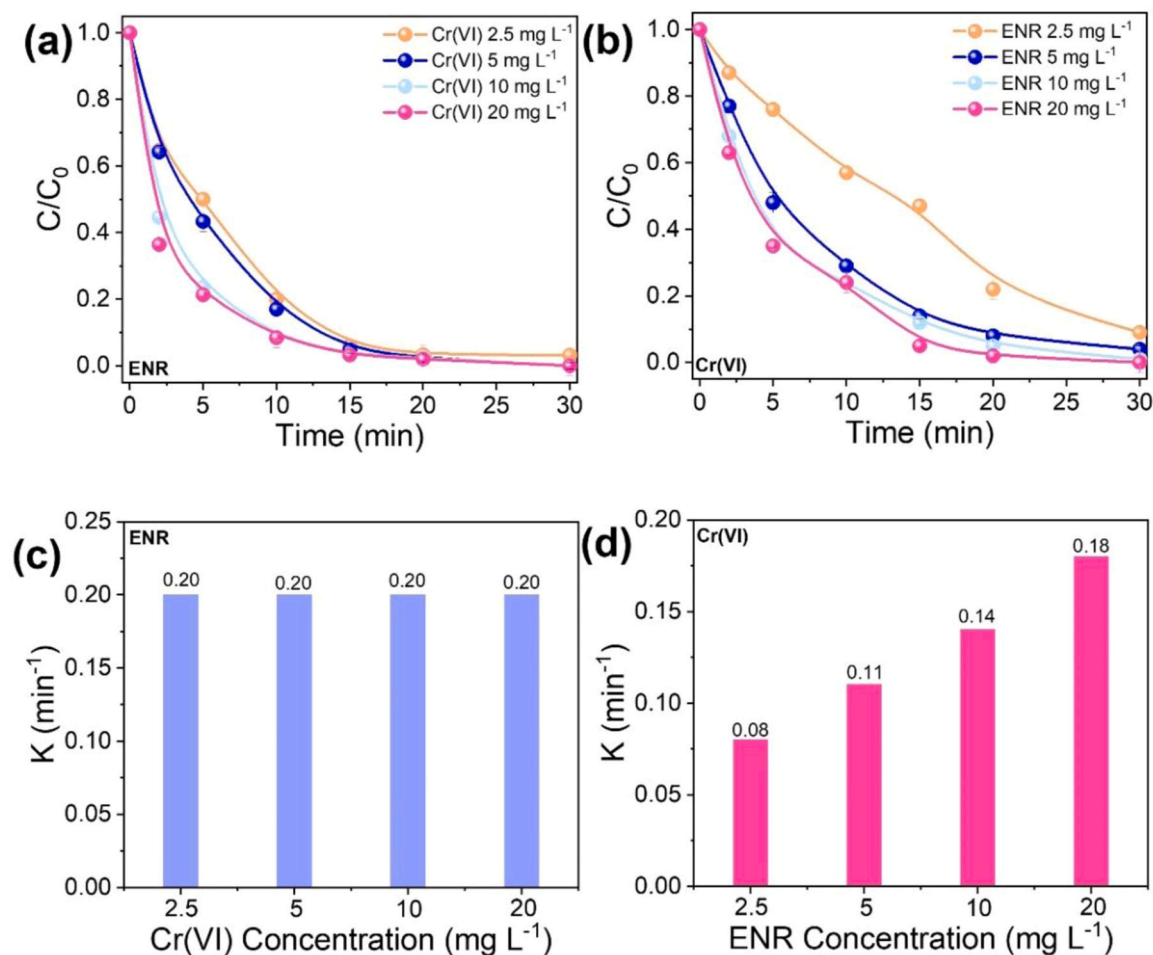

Fig. 8. The removal efficiency and kinetic rate constants under the co-existence of ENR (a, c) and Cr(VI) (b, d) with various initial Cr(VI) and ENR concentrations by C-MoS$_2$-Fe-2/PMS system. (General condition: [catalyst] = 0.2 g L^{-1}, [PMS]$_0$ = 0.2 mM, [ENR]$_0$ = 10 mg L^{-1}, [Cr(VI)]$_0$ = 5 mg L^{-1}, pH 3).

efficiency of Cr(VI) all reached 100% (Fig. 8b), the reaction rate constant increased significantly from 0.08 min^{-1} (2.5 mg L^{-1} ENR) to 0.18 min^{-1} (20 mg L^{-1} ENR) (Fig. 8d). Since the amount of catalyst involved in the reaction did not change at different ENR concentrations, the effect of Fe^{2+} in the catalyst on Cr(VI) reduction was the same, therefore, electron transfer might be a key factor in further promoting Cr(VI) reduction [39]. The charge transfer resistance of C-MoS$_2$-Fe-2 + PMS + ENR was smaller (Fig. S10), which suggested that the charge transfer between C-MoS$_2$-Fe-2-PMS* and ENR was faster [73]. The above electrochemical result demonstrated that C-MoS$_2$-Fe-2 can react with PMS via an electron-mediated process and produce C-MoS$_2$-Fe-2-PMS* complex. C-MoS$_2$-Fe-2-PMS* can increase the redox potential of the catalyst. When the redox potential of the catalyst exceeded the oxidation potential of the ENR, the electrons in ENR will be extracted by C-MoS$_2$-Fe-2-PMS* complex, and the higher the concentration of ENR, the more electrons were extracted, thus promoting the removal of Cr(VI).

3.4. ENR degradation pathways and toxicity

Fukui index based on DFT was first employed to predict the reaction sites of the ROS attacking for ENR molecule (Fig. 9a−d). According to the results, The C1, C8, C10, N18, and N31 positions exhibited higher f$^-$ values, which indicated that these sites were more likely to be attacked in an electrophilic reaction. The C4, C7, C9, and C12 positions of ENR exhibited higher f$^+$ values than others, which translated to these sites being more vulnerable to attack for nucleophilic addition reactions [74, 75]. Then, the intermediates of ENR degradation were analyzed using LC-MS/MS, and the results were exhibited in Table S6 and Fig. S11a−l. Two possible degradation pathways of ENR were proposed by DFT calculations and intermediate product information (Fig. 9e), Pathway I: F atoms in the ENR (A: $m/z = 360$) were substituted by −OH under the attack of ROS. After that, the ring cleavage reaction and decarboxylation were taken place to produce compounds B ($m/z = 358$) and C ($m/z = 334$). Further, the N18 was attacked to form the D ($m/z = 251$) product. Finally, the loss of a piperazine group and decarboxylation yielded E ($m/z = 139$) and F ($m/z = 111$). Pathway II: G ($m/z = 390$) and H ($m/z = 362$) were produced when the F atom was substituted; the
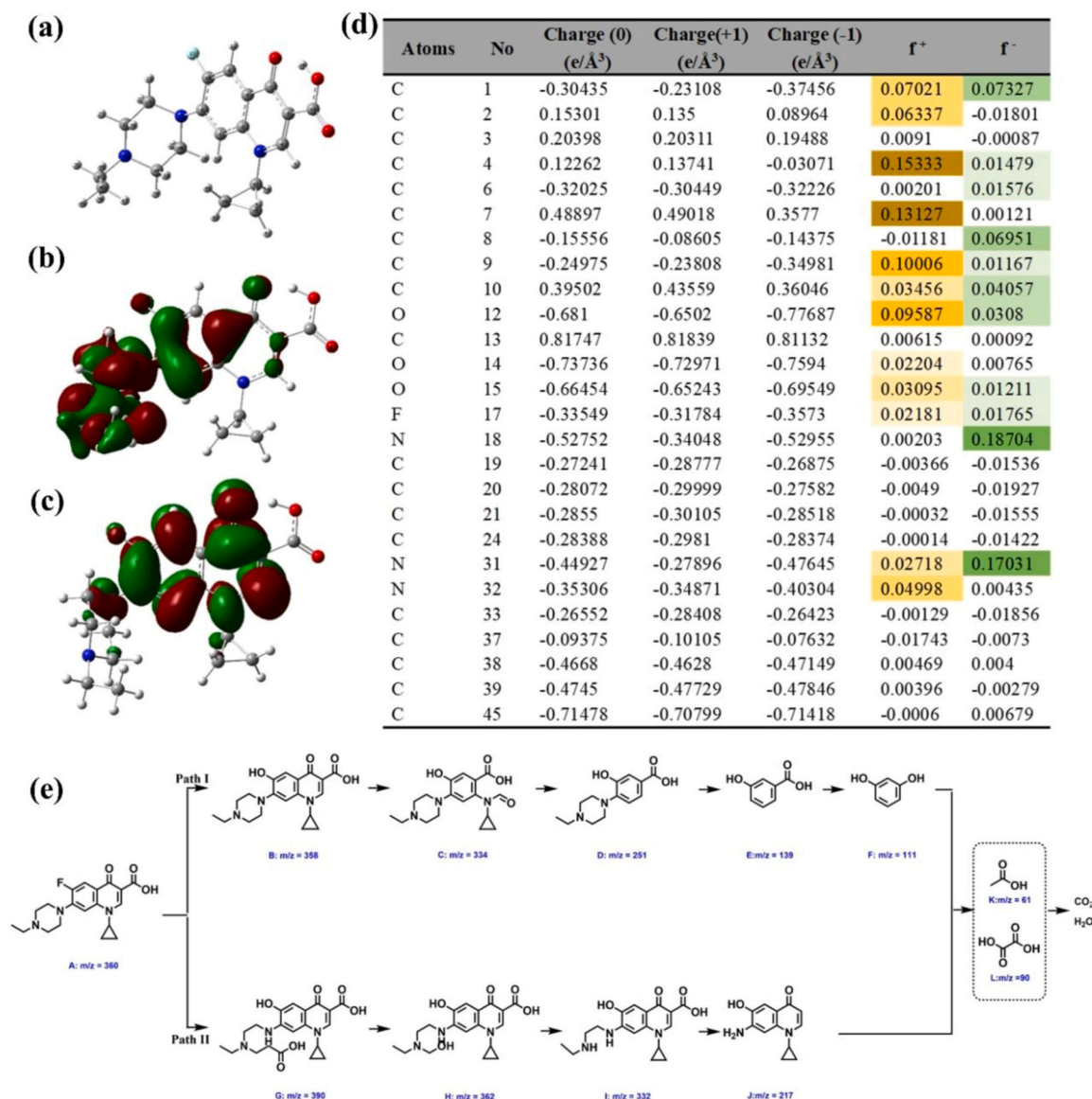

Atoms	No	Charge (0) (e/Å³)	Charge(+1) (e/Å³)	Charge (−1) (e/Å³)	f⁺	f⁻
C	1	-0.30435	-0.23108	-0.37456	0.07021	0.07327
C	2	0.15301	0.135	0.08964	0.06337	-0.01801
C	3	0.20398	0.20311	0.19488	0.0091	-0.00087
C	4	0.12262	0.13741	-0.03071	0.15333	0.01479
C	6	-0.32025	-0.30449	-0.32226	0.00201	0.01576
C	7	0.48897	0.49018	0.3577	0.13127	0.00121
C	8	-0.15556	-0.08605	-0.14375	-0.01181	0.06951
C	9	-0.24975	-0.23808	-0.34981	0.10006	0.01167
C	10	0.39502	0.43559	0.36046	0.03456	0.04057
O	12	-0.681	-0.6502	-0.77687	0.09587	0.0308
C	13	0.81747	0.81839	0.81132	0.00615	0.00092
O	14	-0.73736	-0.72971	-0.7594	0.02204	0.00765
O	15	-0.66454	-0.65243	-0.69549	0.03095	0.01211
F	17	-0.33549	-0.31784	-0.3573	0.02181	0.01765
N	18	-0.52752	-0.34048	-0.52955	0.00203	0.18704
C	19	-0.27241	-0.28777	-0.26875	-0.00366	-0.01536
C	20	-0.28072	-0.29999	-0.27582	-0.0049	-0.01927
C	21	-0.2855	-0.30105	-0.28518	-0.00032	-0.01555
C	24	-0.28388	-0.2981	-0.28374	-0.00014	-0.01422
N	31	-0.44927	-0.27896	-0.47645	0.02718	0.17031
N	32	-0.35306	-0.34871	-0.40304	0.04998	0.00435
C	33	-0.26552	-0.28408	-0.26423	-0.00129	-0.01856
C	37	-0.09375	-0.10105	-0.07632	-0.01743	-0.0073
C	38	-0.4668	-0.4628	-0.47149	0.00469	0.004
C	39	-0.4745	-0.47729	-0.47846	0.00396	-0.00279
C	45	-0.71478	-0.70799	-0.71418	-0.0006	0.00679

Fig. 9. Ball-and-stick model (a), HOMO (b), and LUMO (c) of ENR. Natural population analysis (NPA) charge and calculated Fukui index distribution (f$^+$ and f$^-$) (d). Probable pathways of ENR removal in C-MoS$_2$-Fe/PMS system (e).

piperazine ring was then oxidized and opened to produce I ($m/z = 332$). Subsequently, a decarboxylation reaction occurred, and J ($m/z = 217$) was subsequently generated, after which N31 was oxidized. Finally, the formed compounds of F, and J would undergo the cleavage of piperazine rings to produce a series of small molecules K ($m/z = 61$) and L ($m/z = 90$), and further decarboxylated to eventually mineralize into CO_2 and H_2O [76].

To evaluate the toxicity of ENR and its intermediates, fathead minnow LC50, daphnia magna LD50, bioaccumulation factor, and mutagenicity were predicted by Quantitative Structure Activity Relationship (QSAR) using the Toxicity Evaluation Software Tool (T.E.S.T).

As shown in Fig. S12a, the LC50 of fathead minnow was 0.16 mg L^{-1} for ENR, which can be considered as "High toxic", and as the reaction proceeded, the LC50 of the deep oxidation products K and L became "non-toxic" to fathead minnow (fathead minnow index indexes were 762.37 and 702.23 mg L^{-1}, respectively). DNR with a daphnia magna LD50 value of 2.31 mg L^{-1}, was recognized as a medium toxic chemical (Fig. S12b). All ENR intermediates turned to "low toxic" or "non-toxic" after the reaction. Fig. S12c revealed that the system can significantly reduce the bioaccumulation factor of all the intermediates. Fig. S12d illustrated that as the reaction proceeded further, the mutagenicity of ENR reduced to "mutagenicity negative". Though the toxicity of some
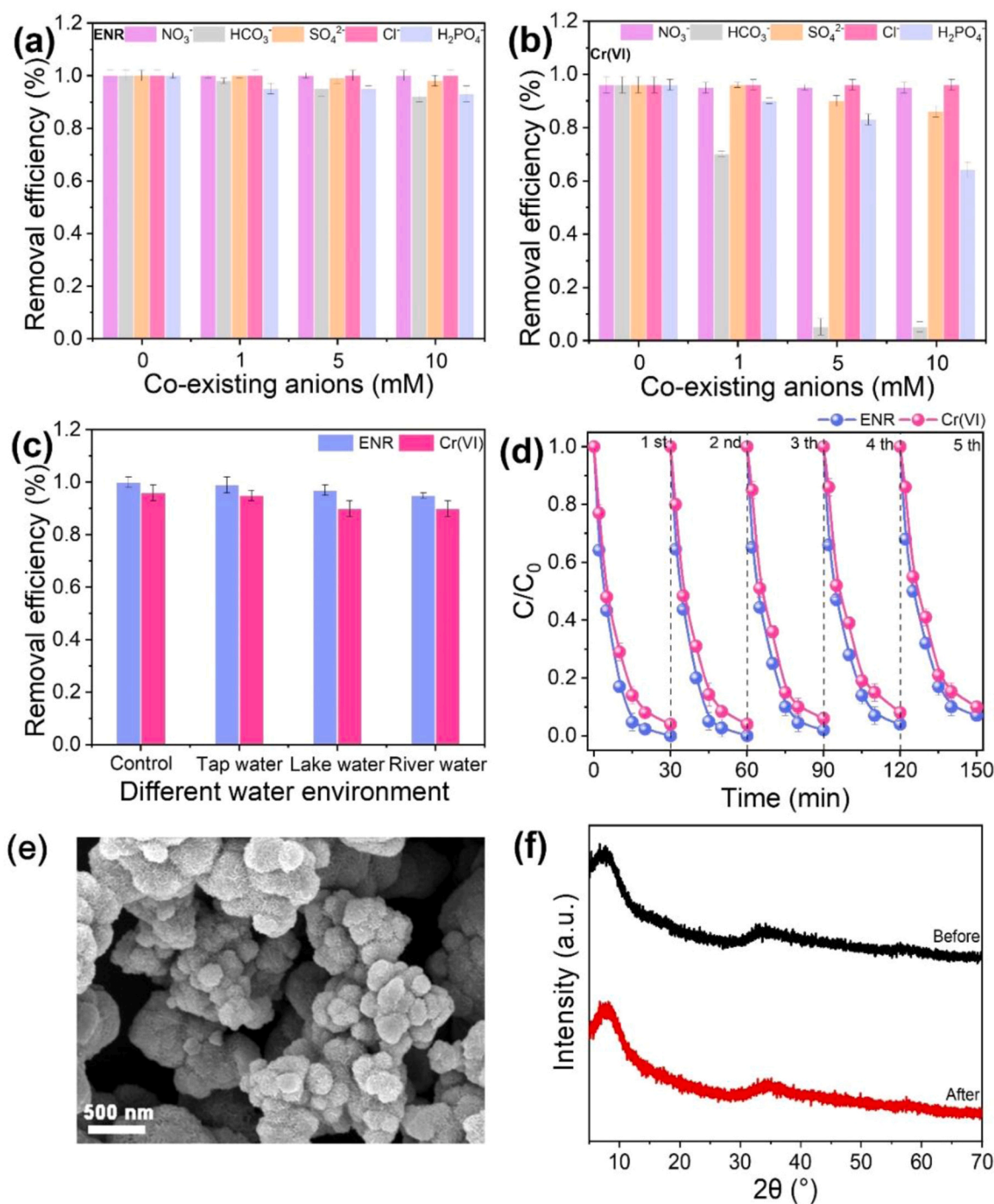

Fig. 10. Effects of NO_3^-, HCO_3^-, SO_4^{2-}, Cl^- and $H_2PO_4^-$ ([anion]$_0$ = 1, 5, 10 mM) on the removal efficiency under co-existence of ENR (a) and Cr(VI) (b) by C-MoS$_2$-Fe-2/PMS system. Different water environment (c) on the removal efficiency under the co-existence of ENR and Cr(VI) by C-MoS$_2$-Fe-2/PMS system. Removal efficiency of ENR and Cr(VI) reused five times (d). SEM image of C-MoS$_2$-Fe-2 after reaction (e). XRD patterns of C-MoS$_2$-Fe-2 before and after reaction (f).

ENR intermediates was higher than that of the parent compound, these results were adequate to demonstrate that the proposal of the system had a general toxicity attenuation effect and was a green ENR degradation technology. As shown in Fig. S13, the TOC removal efficiency of the C-MoS$_2$-Fe-2/PMS system within 30 min is 100.0%, suggesting that ENR can be effectively mineralized. The above results illustrate that the C-MoS$_2$-Fe-2 catalyst not only effectively activated the PMS to remove contaminants, but also effectively reduced the toxicity as well as TOC residual rate of the contaminants.

3.5. Potential application evaluation

The effect of inorganic anions such as NO$_3^-$, HCO$_3^-$, SO$_4^{2-}$, Cl$^-$, H$_2$PO$_4^-$ as well as HA on the removal of ENR and Cr(VI) simultaneously by C-MoS$_2$-Fe-2/PMS were discovered. As shown in Fig. 10a, NO$_3^-$, HCO$_3^-$, SO$_4^{2-}$, and Cl$^-$ did not show remarkable effects on the removal of ENR. Generally, Cl$^-$ reacted with SO$_4^{\bullet-}$ and •OH, generating radicals with weak oxidation capacities (e.g., Cl•, Cl$_2^{\bullet-}$, and ClOH$^{\bullet-}$) that inhibit the removal of organic pollutants [77]. Nevertheless, this inhibition was not evident in the system, suggesting that SO$_4^{\bullet-}$ and •OH were not mainly responsible for ENR removal. The efficiency of ENR removal decreased slightly with increasing H$_2$PO$_4^-$ concentration. Previous studies reported that H$_2$PO$_4^-$ has little inhibitory effect on nonradical-dominated catalytic processes [78]. As a result, the removal of ENR was virtually undisturbed by inorganic anions. As shown in Fig. 10b, NO$_3^-$, SO$_4^{2-}$, and Cl$^-$ had little effect on the removal of Cr(VI). However, with the increase of HCO$_3^-$ concentration, the removal efficiency of Cr(VI) decreased significantly. Partial hydrolysis of HCO$_3^-$ increased the solution pH, thus further inhibiting the removal of Cr(VI) [79]. The removal efficiency of Cr(VI) decreased significantly with increasing H$_2$PO$_4^-$ concentration, which may be attributed to the passivation of the reaction site. Moreover, the introduction of different concentrations of HA did not show remarkable effects on both ENR and Cr(VI) removal (Fig. S14). The above analysis indicated that the system had an excellent anti-interference capacity. In addition, the effects of different water environment on the removal effect of the co-existence of ENR and Cr(VI) were tested. More than 95.0% and 90.0% of ENR and Cr(VI) were removed in all systems (Fig. 10c).

The removal effect of co-existence of other heavy metal ions (Cu(II) or Ni(II)) and ENR by C-MoS$_2$-Fe-2/PMS system was also investigated. As shown in Fig. S15a and c, ENR was rapidly degraded while Cu(II) was efficiently reduced to Cu(I) in ENR and Cu(II) co-existence system. Trace Cu(II) can react with PMS to produce oxidizing Cu(III) [80]. However, the degradation of organic by Cu(III) requires a large amount of PMS and alkaline conditions [80]. And Chi et al. reported that Cu(II)/PMS could hardly degrade the target pollutant under acidic condition [81]. Therefore, Cu(II) tended to be adsorbed and reduced by C-MoS$_2$-Fe-2 [82,83]. The generated Cu(I) can achieve efficient activation of PMS and generate highly reactive radicals that further facilitate the removal of ENR [81,84]. Meanwhile, the presence of e$^-$ in C-MoS$_2$-Fe-2/PMS system can also provide the special conditions with an efficient Cu(II)/Cu(I) reduction cycle [85]. Fig. S15b and d showed the removal effect of co-existence of ENR and Ni(II) by C-MoS$_2$-Fe-2/PMS. Both ENR and Ni(II) were removed to a certain extent. Generally, Ni(II) activation of PMS requires a high concentration of Ni(II) and a large amount of PMS [86]. So Ni(II) tended to be reduced to Ni(0) in C-MoS$_2$-Fe-2/PMS [87].

To verify the stability and reusability of C-MoS$_2$-Fe-2/PMS, 5 cycles of experiments were performed. As illustrated in Fig. 10d, the removal efficiency of the co-existence of ENR and Cr(VI) is 100.0% and 96.0% (1st run); 100.0% and 96.0% (2nd run); 98.2% and 94.3% (3rd run); 96.3% and 92.0% (4th run); 93.0% and 90.0% (5th run), respectively. Moreover, the morphology (Fig. 10e) and XRD patterns (Fig. 10f) of the catalyst before and after catalysis remained almost unchanged, suggesting that the morphology of the catalyst was unchanged and the skeleton structure was maintained well. Therefore, the system showed excellent reusability in the removal of pollutants. During the reaction,

1.8 mg L^{-1} Mo was released, accounting for 0.009% of the total Mo content in catalyst, and 0.26 mg L^{-1} Fe was released. These results further demonstrated the safety of the catalyst in the use process.

More importantly, C-MoS$_2$-Fe-2 was used to activate PMS for the treatment of real pharmaceutical wastewater in order to further evaluate the potential of the system in complex aqueous environments, and some of the conventional water quality indicators were shown in Table S7. The COD of the original water sample was 9120 mg L^{-1}, which was reduced to 7680 mg L^{-1} after 30 min of reaction, and further reduced to 6816 mg L^{-1} after 60 min of reaction. Furthermore, as shown in Fig. S16, the chromaticity of the water samples decreased significantly from the initial 64 to 4 after 60 min of reaction. Therefore, the C-MoS$_2$-Fe-2/PMS system demonstrated excellent treatment effects on real pharmaceutical wastewater.

4. Conclusions

In summary, ethylene glycol was introduced to induce the preparation of 1 T/2 H mixed-phase defect-rich carbon-doped MoS$_2$-Fe (C-MoS$_2$-Fe-x) using a hydrothermal method. Benefitting from the synergistic effect of the introduction of 1 T phase and abundant S defects, C-MoS$_2$-Fe-x had an excellent ability to synchronously remove ENR and Cr (VI) via PMS activation. Experiments and DFT calculations showed that C doping changed the surface charge distribution of MoS$_2$-Fe and increased the conductivity and reactivity of the catalyst, thus favoring the activation of PMS. In addition, the large number of Mo^{4+} sites exposed to C-MoS$_2$-Fe promoted the self-Fe^{2+}/Fe^{3+} cycling of the catalyst, ensuring the number of active sites involved in the reaction. Quenching experiments, EPR tests, and electrochemical experiments revealed the effects of ^{1}O$_2$ as the main ROS and electron transfer on synergistic removal ENR and Cr(VI) in the system. The system still maintained a certain degree of removal efficiency for pollutants under the influence of different environmental factors. In addition, the C-MoS$_2$-Fe-2/PMS system was able to purify real pharmaceutical wastewater with considerable efficiency. The present study provided a new idea for the development of efficient green non-homogeneous catalysts combining homogeneous iron ions and inorganic co-catalysts, and the constructed C-MoS$_2$-Fe-2/PMS exhibited certain practicability for the treatment of real pharmaceutical wastewater.

CRediT authorship contribution statement

Liu Jingyu: Writing – original draft, Software, Methodology, Investigation, Formal analysis. **Hu Yongyou:** Writing – review & editing, Supervision, Funding acquisition, Conceptualization. **Li Xian:** Software. **Xiao Chun:** Software. **Yuan Bowen:** Software. **Cheng Jianhua:** Funding acquisition. **Chen Yuancai:** Funding acquisition. **Zhu Xiaoqiang:** Project administration. **Wang Guobin:** Resources, Project administration. **Xie Jieyun:** Project administration.

Declaration of Competing Interest

The authors declare that there are no competing financial interests or personal relationships that could have appeared to influence the work reported in this paper.

Data Availability

The data that has been used is confidential.

Acknowledgments

Appendix A. Supporting information

Supplementary data associated with this article can be found in the online version at doi:10.1016/j.apcatb.2024.123818.

References

[1] J.X. Nie, S.W. Yan, L.S. Lian, V.K. Sharma, W.H. Song, Development of fluorescence surrogates to predict the ferrate(VI) oxidation of pharmaceuticals in wastewater effluents, Water Res 185 (2020) 116256.

[2] Y.Y. Wu, X.T. Chen, J.C. Cao, Y.Q. Zhu, W.J. Yuan, Z.F. Hu, Z.M. Ao, W.B. Gary, F. H. Tian, J.C. Yu, C.H. Li, Photocatalytically recovering hydrogen energy from wastewater treatment using MoS$_2$@TiO$_2$ with sulfur/oxygen dual-defect, Appl. Catal. B 303 (2022) 120878.

[3] Z.-H. Diao, X.-R. Xu, D. Jiang, J.-J. Liu, L.-J. Kong, G. Li, L.-Z. Zuo, Q.-H. Wu, Simultaneous photocatalytic Cr(VI) reduction and ciprofloxacin oxidation over TiO$_2$/Fe^0 composite under aerobic conditions: performance, durability, pathway and mechanism, Chem. Eng. J. 315 (2017) 167–176.

[4] S.J. Liu, X.F. Zhou, C.H. Wei, Y. Hu, Spatial directional separation and synergetic treatment of Cr(VI) and Rhodamine B mixed pollutants on three-layered Pd@MIL-101/P25 photocatalyst, Sci. Total Environ. 842 (2022) 156836.

[5] Q. Zhang, J. Chen, X. Gao, H.A. Che, P.F. Wang, Y.H. Ao, In-depth insight into the mechanism on photocatalytic synergistic removal of antibiotics and Cr (VI): The decisive effect of antibiotic molecular structure, Appl. Catal. B Environ. 313 (2022) 121443.

[6] Z. Cao, L.X. Zhao, Y.B. Sun, J.W. Feng, Simultaneous removal of enrofloxacin and Cr(VI) using uniaxial wet wall dielectric barrier discharge plasma, J. Clean. Prod. 379 (2022) 134800.

[7] J. Ding, Y. Tang, S. Zheng, S. Zhang, H. Xue, Q. Kong, H. Pang, The synthesis of MOF derived carbon and its application in water treatment, Nano Res 15 (2022) 6793–6818.

[8] Z.-H. Xie, H.-Y. Zhou, C.-S. He, Z.-C. Pan, G. Yao, B. Lai, Synthesis, application and catalytic performance of layered double hydroxide based catalysts in advanced oxidation processes for wastewater decontamination: a review, Chem. Eng. J. 414 (2021) 128713.

[9] C. Zhao, J. Wang, X. Chen, Z. Wang, H. Ji, L. Chen, W. Liu, C.-C. Wang, Bifunctional Bi$_{12}$O$_{17}$Cl$_2$/MIL-100(Fe) composites toward photocatalytic Cr(VI) sequestration and activation of persulfate for bisphenol A degradation, Sci. Total Environ. 752 (2021) 141901.

[10] W.X. Chen, X.W. Xu, J.P. Cui, Z.Y. Zhou, Y.Y. Yao, Porous boron nitride intercalated zero-valent iron particles for highly efficient elimination of organic contaminants and Cr (VI), Chemosphere 306 (2022) 135501.

[11] H. Lan, J. Zhou, Z. Hou, X. An, H. Liu, J. Qu, Defect modulation of MOF-derived ZnFe$_2$O$_4$/CNTs microcages for persulfate activation: Enhanced nonradical catalytic oxidation, Chem. Eng. J. 431 (2022) 133369.

[12] C. Zhao, L.H. Meng, H.Y. Chu, J.-F. Wang, T.Y. Wang, Y.H. Ma, C.-C. Wang, Ultrafast degradation of emerging organic pollutants via activation of peroxymonosulfate over Fe$_3$C/Fe@N-C-x: Singlet oxygen evolution and electron-transfer mechanisms, Appl. Catal. B 321 (2023) 122034.

[13] M. Kohantorabi, G. Moussavi, S. Giannakis, A review of the innovations in metal- and carbon-based catalysts explored for heterogeneous peroxymonosulfate (PMS) activation, with focus on radical vs. non-radical degradation pathways of organic contaminants, Chem. Eng. J. 411 (2021) 127957.

[14] J.Q. Ma, N. Jia, H.X. Jin, S.J. Yao, K.F. Zhang, Y. Kai, W.L. Wu, Y.Z. Wen, Chitosan induced synthesis of few-layer MoS$_2$/Fe-doped biochar and its dual applications in Cr(VI) removal, Sep. Purif. Technol. 317 (2023) 123880.

[15] Y.J. Yao, H.Y. Yin, Y.Y. Zhang, F.Y. Wei, H.W. Hu, Y.H. Tang, S.B. Wang, Fe, Cu-coordinated ZIF-derived bimetal encapsulated N-doped carbon nanotube for efficient remediation of various aqueous pollutants, Chem. Eng. J. 426 (2021) 131801.

[16] Z.J. Xiao, B.Q. Zhou, X.C. Feng, H.T. Shi, Yi.N. Zhu, C.P. Wang, B.V. Bruggen, N. Q. Ren, Anchored Co-oxo generated by cobalt single atoms outperformed aqueous species from the counterparts in peroxymonosulfate treatment, Appl. Catal. B 328 (2023) 122483.

[17] K.X. Yin, R.X. Wu, Y.N. Shang, D.D. Chen, Z.L. Wu, X.H. Wang, B.Y. Gao, X. Xu, Microenvironment modulation of cobalt single-atom catalysts for boosting both radical oxidation and electron-transfer process in Fenton-like system, Appl. Catal. B 329 (2023) 122558.

[18] J. Zhou, X.J. Guo, X. Zhou, J.J. Yang, S.H. Yu, X.Y. Niu, Q.Y. Chen, F. Li, Y.B. Liu, Boosting the efficiency of Fe-MoS$_2$/peroxymonosulfate catalytic systems for organic powllutants remediation: Insights into edge-site atomic coordination, Chem. Eng. J. 433 (2022) 134511.

[19] J.X. Chen, J.Y. Xu, Y.H. Zhong, L.L. Cao, L. Ren, X.L. Zhang, Z.Y. Wang, J.F. Chen, S.T. Lin, Q.Q. Xu, Y.Z. Chen, MoS$_2$ nanoflowers decorated with single Fe atoms catalytically boost the activation properties of peroxymonosulfate, Colloid Surf. A 665 (2023) 131173.

[20] X.N. Wang, X.C. Zhang, Y. Zhang, Y. Wang, S.-P. Sun, W.D. Wu, Z.X. Wu, Nanostructured semiconductor supported iron catalysts for heterogeneous photo-Fenton oxidation: a review, J. Mater. Chem. A 8 (2020) 15513.

[21] Y.B. Sun, R.P. Li, C.L. Song, H. Zhang, Y.C. Cheng, A.M. Nie, H.C. Li, D. D. Dionysiou, J.S. Qian, B.C. Pan, Origin of the improved reactivity of MoS$_2$ single crystal by confining lattice Fe atom in peroxymonosulfate-based Fenton-like reaction, Appl. Catal. B 298 (2021) 120537.

[22] Z.X. Li, M. Sun, J.L. Yang, S. Dong, High-performance iron-doped molybdenum disulfide photocatalysts enhance peroxymonosulfate activation for water decontamination, Chem. Eng. J. 446 (2022) 137380.

[23] S. Wang, D. Zhang, B. Li, C. Zhang, Z. Du, H. Yin, X. Bi, S. Yang, Ultrastable in plane 1T–2H MoS$_2$ heterostructures for enhanced hydrogen evolution reaction, Adv. Energy Mater. 8 (2018) 1801345.

[24] S. Lee, J. Hwang, D. Kim, H. Ahn, Oxygen incorporated in 1T/2H hybrid MoS$_2$ nanoflowers prepared from molybdenum blue solution for asymmetric supercapacitor applications, Chem. Eng. J. 419 (2021) 129701.

[25] H. Li, C. Tsai, A.L. Koh, L. Cai, A.W. Contryman, A.H. Fragapane, J. Zhao, H.S. Han, H.C. Manoharan, F. Abild-Pedersen, Activating and optimizing MoS$_2$ basal planes for hydrogen evolution through the formation of strained sulphur vacancies, Nat. Mater. 15 (2016) 48–53.

[26] G. Li, C. Fu, J. Wu, J. Rao, S.-C. Liou, X. Xu, B. Shao, K. Liu, E. Liu, N. Kumar, X. Liu, M. Fahlman, J. Gooth, G. Auffermann, Y. Sun, C. Felser, B. Zhang, Synergistically creating sulfur vacancies in semimetal-supported amorphous MoS$_2$ for efficient hydrogen evolution, Appl. Catal. B 254 (2019) 1–6.

[27] Y. Li, J. Wang, X.K. Tian, L.L. Ma, C. Dai, C. Yang, Z.X. Zhou, Carbon doped molybdenum disulfide nanosheets stabilized on graphene for hydrogen evolution reaction with high electrocatalytic ability, Nanoscale 8 (2016) 1676–1683.

[28] J.P. Perdew, K. Burke, M. Ernzerhof, Generalized gradient approximation made simple, Phys. Rev. Lett. 77 (1996) 3865–3868.

[29] G. Kresse, D. Joubert, From ultrasoft pseudopotentials to the projector augmented-wave method, Phys. Rev. B 59 (1999) 1758–1775.

[30] P.E. Blöchl, Projector augmented-wave method, Phys. Rev. B 50 (1994) 17953–17979.

[31] X.H. Leng, Y.M. Wang, F. Wang, Alcohols assisted hydrothermal synthesis of defect-rich MoS$_2$ and their applications in humidity sensing, Adv. Mater. Interfaces 6 (2019) 1900010.

[32] S.R. Li, X. Chen, M.J. Li, C. Xue, Y.H. Long, W.H. Liu, Z.H. Cao, X.Q. Tong, W. L. Huang, D.F. Liu, Hollow Co$_3$S$_4$ polyhedron decorated with interlayer-expanded MoS$_2$ nanosheets for efficient tetracycline removal from aqueous solution, Chem. Eng. J. 441 (2022) 136006.

[33] Z.L. Wu, W.K. Song, X.W. Xu, J.N. Yuan, W.Y. Lv, Y.Y. Yao, High 1T phase and sulfur vacancies in C-MoS$_2$@Fe induced by ascorbic acid for synergistically enhanced contaminants degradation, Sep. Purif. Technol. 286 (2022) 120511.

[34] J.C.E. Yang, M.P. Zhu, X.G. Duan, S.B. Wang, B.L. Yuan, M.L. Fu, The mechanistic difference of ^{1}T–^{2}H MoS$_2$ homojunctions in persulfates activation: structure-dependent oxidation pathways, Appl. Catal. B 297 (2021) 120460.

[35] Q. Zhong, C.M. Xu, Y.Z. Liu, Q.Y. Ji, Z. Xu, D.Y. Sun, S.H. Zhou, B. Yang, Y.H. Dai, C.D. Qi, S.G. Yang, H. He, S.Y. Li, C. Sun, Defect-engineered FeSe$_2$-x@C with porous architecture for enhanced peroxymonosulfate-based advanced oxidation processes, Appl. Catal. B 309 (2022) 121259.

[36] Z.Y. Li, R.Y. Fan, Z. Hu, W.C. Li, H.J. Zhou, S.H. Kang, Y.X. Zhang, H.M. Zhang, G. Z. Wang, Ethanol introduced synthesis of ultrastable 1T-MoS$_2$ for removal of Cr (VI), J. Hazard. Mater. 394 (2020) 122525.

[37] J. Bai, B.C. Zhao, J.F. Zhou, J.G. Si, Z.T. Fang, K.Z. Li, H.Y. Ma, J.M. Dai, X.B. Zhu, Y.P. Sun, Glucose-induced synthesis of 1T-MoS$_2$/C hybrid for high-rate lithium-ion batteries, Small 15 (2019) 1805420.

[38] Q.R. Zeng, Z.A. Jia, X. Liu, B.W. Xiu, J.P. Cheng, Multi-interface polarization engineering constructed ^{1}T–^{2}H MoS$_2$ QDs/Y-NaBi(MoO$_4$)$_2$ multiple heterostructure for high-efficient piezoelectric-photoelectrocatalysis PDE-5i degradation, Appl. Catal. B 327 (2023) 122460.

[39] J.Y. Liu, Y.Y. Hu, X. Li, C. Xiao, Y.Y. Shi, Y.C. Chen, J.H. Cheng, X.Q. Zhu, G. B. Wang, J.Y. Xie, High-efficient degradation of chloroquine phosphate by oxygen doping MoS$_2$ co-catalytic Fenton reaction, J. Hazard. Mater. 458 (2023) 131894.

[40] J.F. Xie, J.J. Zhang, S. Li, F. Grote, X.D. Zhang, H. Zhang, R.X. Wang, Y. Lei, B. C. Pan, Y. Xie, Controllable disorder engineering in oxygen-incorporated MoS$_2$ ultrathin nanosheets for efficient hydrogen evolution, J. Am. Chem. Soc. 135 (2013) 17881–17888.

[41] Q.Y. Yan, C. Lian, K. Huang, L.H. Liang, H.R. Yu, P.C. Yin, J.L. Zhang, M.Y. Xing, Constructing an acidic microenvironment by MoS$_2$ in heterogeneous Fenton reaction for pollutant control, Angew. Chem. Int. Ed. 60 (2021) 17155–17163.

[42] G. Bharath, K. Rambabu, P.P. Morajkar, R. Jayaraman, J. Theerthagiri, S.J. Lee, M. Y. Choi, F. Banat, Surface functionalized highly porous date seed derived activated carbon and MoS$_2$ nanocomposites for hydrogenation of CO$_2$ into formic acid, J. Hazard. Mater. 409 (2021) 124980.

[43] Y. Yang, Q.Q. Wang, R. Aleisa, T.T. Zhao, S.H. Ma, G.X. Zhang, T.J. Yao, Y.D. Yin, MoS$_2$/FeS nanocomposite catalyst for efficient Fenton reaction, ACS Appl. Mater. Interfaces 13 (2021) 51829–51838.

[44] Q. Tang, Tuning the phase stability of Mo-based TMD monolayers through coupled vacancy defects and lattice strain, J. Mater. Chem. C. 6 (2018) 9561–9568.

[45] Q. Jin, N. Liu, B.H. Chen, D.H. Mei, Mechanisms of semiconducting 2H to metallic 1T phase transition in two-dimensional MoS$_2$ nanosheets, J. Phys. Chem. C. 122 (2018) 28215–28224.

[46] T. Tian, X.Y. Jin, N. Guo, H.Q. Li, Y. Han, Y.P. Yuan, CdS/ethylenediamine nanowires 3D photocatalyst with rich sulfur vacancies for efficient syngas production from CO$_2$ photoreduction, Appl. Catal. B 308 (2022) 121227.

[47] X. Li, Y. Guo, L. Yan, T. Yan, W. Song, R. Feng, Y. Zhao, Enhanced activation of peroxymonosulfate by ball-milled MoS$_2$ for degradation of tetracycline: boosting molybdenum activity by sulfur vacancies, Chem. Eng. J. 429 (2022) 132234.

[48] J. Lu, Y.J. Zhou, Y.B. Zhou, Efficiently activate peroxymonosulfate by Fe$_3$O$_4$@MoS$_2$ for rapid degradation of sulfonamides, Chem. Eng. J. 422 (2021) 130126.

[49] H. Mao, Y.L. Fu, H.R. Yang, Z.-Z. Deng, Y. Sun, D.L. Liu, Q. Wu, T.Y. Ma, X.-M. Song, Ultrathin 1T-MoS$_2$ nanoplates induced by quaternary ammonium-type ionic liquids on polypyrrole/graphene oxide nanosheets and its irreversible crystal

phase transition during electrocatalytic nitrogen reduction, ACS Appl. Mater. Interfaces 12 (2020) 25189–25199.

[50] K.Y. Qi, Z.M. Yuan, Y. Hou, R.C. Zhao, B.W. Zhang, Facile synthesis and improved Li-storage performance of Fe-doped MoS₂/reduced graphene oxide as anode materials, Appl. Surf. Sci. 483 (2019) 688–695.

[51] Z. Ye, J.A. Padilla, E. Xuriguera, J.L. Beltran, F. Alcaide, E. Brillas, I. Sirés, A highly stable metal-organic framework-engineered FeS₂/C nanocatalyst for heterogeneous electro-Fenton treatment: validation in wastewater atmild pH, Environ. Sci. Technol. 54 (2020) 4664–4674.

[52] C.C. Dong, J.H. Ji, B. Shen, M.Y. Xing, J.L. Zhang, Enhancement of H₂O₂ decomposition by the co-catalytic effect of WS₂ on the Fenton reaction for thesynchronous reduction of Cr(VI) and remediation of phenol, Environ. Sci. Technol. 52 (2018) 11297–11308.

[53] M. Kohantorabi, G. Moussavi, S. Giannakis, A review of the innovations in metal- and carbon-based catalysts explored for heterogeneous peroxymonosulfate (PMS) activation, with focus on radical vs. non-radical degradation pathways of organic contaminants, Chem. Eng. J. 411 (2021) 127957.

[54] Y. Zhang, S.-J. Park, Facile construction of MoO₃@ZIF-8 core-shell nanorods for efficient photoreduction of aqueous Cr (VI), Appl. Catal. B 240 (2019) 92–101.

[55] T. Guo, L.S. Jiang, H.X. Huang, Y. Li, X.Y. Wu, G.K. Zhang, Enhanced degradation of tetracycline in water over Cu-doped hematite nanoplates by peroxymonosulfate activation under visible light irradiation, J. Hazard. Mater. 416 (2021) 125838.

[56] X. Wang, Y.W. Zhang, H.N. Si, Q.H. Zhang, J. Wu, L. Gao, X.F. Wei, Y. Sun, Q. L. Liao, Z. Zhang, K. Ammarah, L. Gu, Z. Kang, Y. Zhang, Single-atom vacancy defect to trigger high-efficiency hydrogen evolution of MoS₂, J. Am. Chem. Soc. 142 (2020) 4298–4308.

[57] L.D. Liu, Q. Liu, Y. Wang, J. Huang, W. Wang, L. Duan, X. Yang, X.Y. Yu, X. Han, N. Liu, Nonradical activation of peroxydisulfate promoted by oxygen vacancy-laden NiO for catalytic phenol oxidative polymerization, Appl. Catal. B 254 (2019) 166–173.

[58] S. Guo, H.J. Wang, W. Yang, H. Fida, L. You, K. Zhou, Scalable synthesis of Ca-doped α-Fe₂O₃ with abundant oxygen vacancies for enhanced degradation of organic pollutants through peroxymonosulfate activation, Appl. Catal. B 262 (2020) 118250.

[59] X. Liu, J. Wang, D. Wu, Z. Wang, Y. Li, X. Fan, F. Zhang, G. Zhang, W. Peng, N-doped carbon dots decorated 3D g-C₃N₄ for visible-light driven peroxydisulfate activation: Insights of non-radical route induced by Na⁺ doping, Appl. Catal. B 310 (2022) 121304.

[60] J.L. Niu, R.X. Hu, L.W. Tang, Y.X. Huang, J.H. Cheng, Y.Y. Hu, In-situ growth of C-F@CCS@ZIF8/67–1/1 photocatalysts with internal electric field and interfacial enhancement on cobalt-copper foam surface for simultaneous removal of ciprofloxacin and Cr(VI), Appl. Catal. B 334 (2023) 122857.

[61] L.K. Chen, Y.F. Huang, M.L. Zhou, K.W. Xing, W.Y. Lv, W.T. Wang, H.X. Chen, Y. Y. Yao, Nitrogen-doped porous carbon encapsulating iron nanoparticles for enhanced sulfathiazole removal via peroxymonosulfate activation, Chemosphere 250 (2020) 126300.

[62] F. Wang, J. Xu, Z.P. Wang, Y. Lou, C.S. Pan, Y.F. Zhu, Unprecedentedly efficient mineralization performance of photocatalysis-self-Fenton system towards organic pollutants over oxygen-doped porous g-C₃N₄ nanosheets, Appl. Catal. B 312 (2022) 121438.

[63] R. Ji, Y.M. Dong, H. Zhao, C.S. Pan, G.L. Wang, Y.F. Zhu, J.S. Li, Z-scheme cobalt-iron oxide/perylene diimide supermolecule heterojunction for high-efficiency ciprofloxacin removal in a photocatalysis-self-Fenton system, J. Colloid Interf. Sci. 648 (2023) 623–632.

[64] S. Chen, B. Li, D.L. Huang, P. Xu, Y.S. Chen, L. Lei, Z.W. Wang, R. Deng, L. Du, G. F. Wang, Jointed synchronous photocatalytic oxidation and chromate reduction enabled by the defect distribution upon BiVO₄: mechanism insight and toxicity assessment, ACS Appl. Mater. Interfaces 13 (2021) 17586–17598.

[65] H.Y. Luo, H.Y. Fu, H. Yin, Q.T. Lin, Carbon materials in persulfate-based advanced oxidation processes: the roles and construction of active sites, J. Hazard. Mater. 426 (2022) 128044.

[66] X.J. Tan, W.H. Ding, Z.Y. Jiang, L.X. Sun, Y.X. Huang, Reinventing MoS₂ co-catalytic Fenton reaction: oxygen-incorporation mediating surface superoxide radical generation, Nano Res. 15 (2021) 1973–1982.

[67] Y.F. Xiao, J.H. Ji, L.L. Zhu, Y. Bao, X.Y. Liu, J.L. Zhang, M.Y. Xing, Regeneration of zero-valentiron powder by the cocatalytic effect of WS₂ in the environmental applications, Chem. Eng. J. 383 (2020) 123158.

[68] J.Q. Li, M.T. Li, H.Q. Sun, Z.M. Ao, S.B. Wang, S.M. Liu, Understanding of the oxidation behavior of benzyl alcohol by peroxymonosulfate via carbon nanotubes activation, ACS Catal. 10 (2020) 3516–3525.

[69] N. Li, R. Li, X. Duan, B. Yan, W. Liu, Z. Cheng, G. Chen, La Hou, S. Wang, Correlation of active sites to generated reactive species and degradation routes of organics in peroxymonosulfate activation by co-loaded carbon, Environ. Sci. Technol. 55 (2021) 16163–16174.

[70] H. Meng, C. Nie, W. Li, X. Duan, B. Lai, Z. Ao, S. Wang, T. An, Insight into the effect of lignocellulosic biomass source on the performance of biochar as persulfate activator for aqueous organic pollutants remediation: Epicarp and mesocarp of citrus peels as examples, J. Hazard. Mater. 399 (2020) 123043.

[71] W. Liu, C. Nie, W. Li, Z. Ao, S. Wang, T. An, Oily sludge derived carbons as peroxymonosulfate activators for removing aqueous organic pollutants: Performances and the key role of carbonyl groups in electron-transfer mechanism, J. Hazard. Mater. 414 (2021) 125552.

[72] L.Y. Wu, P.P. Guo, X. Wang, H.Y. Li, A.Z. Li, K.Y. Chen, Mechanism study of CoS₂/Fe(III)/peroxymonosulfate catalysis system: the vital role of sulfur vacancies, Chemosphere 288 (2022) 132646.

[73] T. Yang, S.S. Fan, Y. Li, Q. Zhou, Fe-N/C single-atom catalysts with high density of Fe-Nx sites toward peroxymonosulfate activation for high-efficient oxidation of bisphenol A: Electron-transfer mechanism, Chem. Eng. J. 419 (2021) 129590.

[74] T.S. Chen, Q.X. Zhang, Z.J. Xie, C.W. Tan, P. Chen, Y.Q. Zeng, F.L. Wang, H.J. Liu, Y. Liu, G.G. Liu, W.Y. Lv, Carbon nitride modified hexagonal boron nitride interface as highly efficient blue LED light-driven photocatalyst, Appl. Catal. B-Environ. 238 (2018) 410–421.

[75] J.X. Huang, D.G. Li, R.B. Li, P. Chen, Q.X. Zhang, H.J. Liu, W.Y. Lv, G.G. Liu, Y. P. Feng, One-step synthesis of phosphorus/oxygen co-doped g-C₃N₄/anatase TiO₂ Z-scheme photocatalyst for significantly enhanced visible-light photocatalysis degradation of enrofloxacin, J. Hazard. Mater. 386 (2020) 121634–121646.

[76] X. Li, C. Xiao, X. Ruan, Y.Y. Hu, C.Y. Zhang, J.H. Cheng, Y.C. Chen, Enrofloxacin degradation in a heterogeneous electro-Fenton system using a tri-metal-carbon nanofibers composite cathode, Chem. Eng. J. 427 (2022) 130927.

[77] C. Zhao, J. Wang, X. Chen, Z. Wang, H. Ji, L. Chen, W. Liu, C.-C. Wang, Bifunctional Bi₁₂O₁₇Cl₂/MIL-100(Fe) composites toward photocatalytic Cr(VI) sequestration and activation of persulfate for bisphenol A degradation, Sci. Total Environ. 752 (2021) 141901.

[78] X. Duan, Z. Ao, L. Zhou, H. Sun, G. Wang, S. Wang, Occurrence of radical and nonradical pathways from carbocatalysts for aqueous and nonaqueous catalytic oxidation, Appl. Catal. B 188 (2016) 98–105.

[79] L. Lai, H. Ji, H. Zhang, R. Liu, C. Zhou, W. Liu, Z. Ao, N. Li, C. Liu, G. Yao, Activation of peroxydisulfate by V-Fe concentrate ore for enhanced degradation of carbamazepine: surface≡V(III) and≡V(IV) as electron donors promoted the regeneration of≡Fe(II), Appl. Catal. B 282 (2021) 19559.

[80] L. Wang, H. Xu, N. Jiang, Z. Wang, J. Jiang, T. Zhang, Trace cupricspecies triggered decomposition of peroxymonosulfate and degradation of organic pollutants: Cu(III) being the primary and selective intermediate oxidant, Environ. Sci. Technol. 54 (2020) 4686–4694.

[81] H. Chi, X. He, J. Zhang, D. Wang, X. Zhai, J. Ma, Hydroxylamine enhanced degradation of naproxen in Cu²⁺ activated peroxymonosulfate system at acidic condition: efficiency, mechanisms and pathway, Chem. Eng. J. 361 (2019) 764–772.

[82] Q.Y. Yi, J.H. Ji, B. Shen, C.C. Dong, J. Liu, J.L. Zhang, M.Y. Xing, Singlet oxygen triggered by superoxide radicals in amolybdenum cocatalytic Fenton reaction with enhanced REDOX activity in the environment, Environ. Sci. Technol. 53 (2019) 9725–9733.

[83] J.B. Dan, P.H. Rao, Q.F. Wang, L. Dong, W.H. Chu, M. Zhang, Z.D. He, N.Y. Gao, J. Deng, J.X. Chen, MgO-supported CuO with encapsulated structure for enhanced peroxymonosulfate activation to remove thiamphenicol, Sep. Purif. Technol. 280 (2022) 119782.

[84] X. Zhou, H. Luo, B. Sheng, X. Chen, Y. Wang, Q. Chen, J. Zhou, Cu²⁺/Cu⁺ cycle promoted PMS decomposition with the assistance of Mo for the degradation of organic pollutant, J. Hazard. Mater. 411 (2021) 125050.

[85] B. Zhang, Z.W. Han, Y.J. Xin, Y.J. Zhang, W.Q. Li, B.D. Li, A. Ding, J. Ma, X. He, Peroxymonosulfate activation by vacuum ultraviolet and trace copper ions: a new way to boost Cu(II)/Cu(I) redox cycle, Chem. Eng. J. 450 (2022) 138097.

[86] Y. Lu, F.J. Yang, S.Y. Chen, W.C. Shi, C.D. Qi, G.L. Peng, Decomplexation of Ni(II)-citrate and recovery of nickel from chelated nickel containing electroplating wastewater by peroxymonosulfate with nickel, Sep. Purif. Technol. 283 (2022) 120142.

[87] H. Singh, A. Rai, R. Yadav, A.K. Sinha, Glucose hydrogenation to sorbitol over unsupported mesoporous Ni/NiO catalyst, Mol, Catal 451 (2018) 186–191.